

# Settling velocity and concentration distribution of heavy particles in homogeneous isotropic turbulence

By LIAN-PING WANG† AND MARTIN R. MAXEY

Center for Fluid Mechanics, Turbulence, and Computation, Box 1966, Brown University,  
Providence, RI 02912, USA

(Received 25 November 1992 and in revised form 17 April 1993)

The average settling velocity in homogeneous turbulence of a small rigid spherical particle, subject to a Stokes drag force, has been shown to differ from that in still fluid owing to a bias from the particle inertia (Maxey 1987). Previous numerical results for particles in a random flow field, where the flow dynamics were not considered, showed an increase in the average settling velocity. Direct numerical simulations of the motion of heavy particles in isotropic homogeneous turbulence have been performed where the flow dynamics are included. These show that a significant increase in the average settling velocity can occur for particles with inertial response time and still-fluid terminal velocity comparable to the Kolmogorov scales of the turbulence. This increase may be as much as 50% of the terminal velocity, which is much larger than was previously found. The concentration field of the heavy particles, obtained from direct numerical simulations, shows the importance of the inertial bias with particles tending to collect in elongated sheets on the peripheries of local vortical structures. This is coupled then to a preferential sweeping of the particles in downward moving fluid. Again the importance of Kolmogorov scaling to these processes is demonstrated. Finally, some consideration is given to larger particles that are subject to a nonlinear drag force where it is found that the nonlinearity reduces the net increase in settling velocity.

---

## 1. Introduction

A knowledge of the average settling rate of small heavy particles in turbulent flows is important to many multiphase-flow problems involving particle transport and dispersion. Examples include the settling of aerosol particles in the atmosphere or small water droplets in clouds, sediment transport in rivers, transport of dust from soil erosion or ash from volcanic eruptions, and other processes such as the combustion or the mixing of sprays. For the most part, attention has been focused in the past on the dispersion of aerosol particles by homogeneous isotropic turbulence. Theoretical investigations in this area have been made by Yudine (1959), Csanady (1963), Meek & Jones (1973), Reeks (1977, 1980) and Nir & Pismen (1979) amongst others. Yudine (1959) and Csanady (1963) demonstrated the ‘crossing-trajectories effect’ for particles settling under gravity where particles move relative to the surrounding fluid, crossing the trajectories of Lagrangian fluid elements. As a result the turbulent dispersion

† Present address: Department of Mechanical Engineering, Pennsylvania State University, University Park, PA 16802, USA.

decreases as the settling velocity increases. Other authors have investigated the effect of particle inertia on dispersion; these and other results are summarized in the recent papers of Mei, Adrian & Hanratty (1991) and Wang & Stock (1993). Experiments on particle dispersion have been conducted by Snyder & Lumley (1971) and Wells & Stock (1983) and there have been several studies involving numerical simulations such as those by Riley & Patterson (1974), Squires & Eaton (1991*a*), and Yeh & Lei (1991).

Only recently has the question of changes in the average settling velocity in homogeneous turbulence been carefully addressed. Specifically we consider spherical aerosol particles settling in homogeneous and isotropic turbulence where the Eulerian flow field has zero mean. Reeks (1977) has argued that the average settling velocity of heavy particles would be the same as the terminal fall velocity in still fluid (hereinafter referred to as *the terminal velocity*) if the flow velocity is treated as a stochastic random field. It can be rigorously shown that (Maxey 1987), in the absence of particle inertia, the ensemble average velocity of a small spherical particle is indeed the same as the terminal velocity. Furthermore, if the particle inertia is very large, i.e. the particle aerodynamical response time is much greater than any integral timescale of the flow, the fluid velocity seen by a particle appears as an uncorrelated random noise and should again have no net effect on the settling rate. In general any net effect of turbulent motion, either to reduce or enhance the settling rate (relative to the terminal velocity), should occur under the influence of intermediate or finite particle inertia.

The motion of a spherical, aerosol particle is typically governed by the fluid drag force due to the relative motion of the particle to the surrounding fluid, the force of gravity on the particle and the inertia of the particle. For very small particles a linear Stokes drag law may be used to determine the drag force while for a larger particle whose motion relative to the surrounding fluid corresponds to a finite particle Reynolds number, the drag force varies nonlinearly with the relative velocity of the particle to the fluid. Tunstall & Houghton (1968) demonstrated that the interaction of a nonlinear drag force and particle inertia would reduce the average settling velocity in a flow oscillating in time about a zero mean, even without any spatial variation in the flow. By contrast a linear drag force would result in no net change in the settling velocity. The experiments of Tunstall & Houghton (1968) for spherical particles settling in liquids, and later work by Schöneborn (1975) and Hwang (1985) have generally confirmed this reduction in the average settling velocity for simple oscillatory flows, though there is some uncertainty about the theoretical estimates and the appropriate way in which to represent the fluid forces on the sphere. A characteristic of turbulent flows is the strong spatial variations that occur over a wide range of lengthscales. This presents the possibility for strong couplings between the particle motion and the spatial variations in the flow.

As a first step in understanding the settling of finite-inertia particles in turbulent flows, Maxey & Corrsin (1986) studied the motion of aerosol particles in an ensemble of randomly oriented, periodic, cellular flow fields. The particles were subject to a linear Stokes drag force and the flow was spatially non-uniform. They showed that the average settling rate, over a wide range, is larger than the terminal velocity as particles tend to settle in the downward-flow side of a cell. The particles were also found to accumulate along isolated open paths. A more general framework directed toward the settling of heavy particles in turbulent flows was provided by Maxey (1987). An analysis was made for both the limits of rapidly settling particles and particles with weak inertia to determine the changes in the average settling velocity for Stokes particles. A kinematic, random flow field generated from random Fourier modes was used to simulate numerically the motion of aerosol particles in a homogeneous, isotropic

random flow and it was found that for finite particle inertia the average settling velocity was sometimes 10% greater than the terminal velocity. The tendency to an increase in the settling velocity was also verified by the asymptotic analysis. It has been argued that this relative increase is related to an inertial bias that causes particles to accumulate in regions of high flow strain rate or low flow vorticity. This preferential accumulation has been confirmed by the results from full direct numerical simulations for non-settling particles in homogeneous turbulence by Squires & Eaton (1991*b*).

Other studies of particle motion that should be mentioned include Fung (1990) and Yeh & Lei (1991). Fung *et al.* (1992) developed an extended form of the kinematic, random mode, simulation technique which allows for some of the dynamical features of the turbulence to be included and for features such as an inertial subrange to be represented. Fung (1990) applied this to investigate individual particle trajectories of settling particles. Yeh & Lei (1991) employed a large-eddy simulation for decaying, homogeneous, isotropic turbulence and included the motion of heavy particles, using an empirical Reynolds-number-dependent relation to estimate the drag force on the particles. The results were limited but indicated an increase of about 5% in the average settling velocity. The first objectives of this present study are to verify from direct numerical simulations of homogeneous, isotropic turbulence that aerosol particles subjected to a linear Stokes drag do settle on average more rapidly and to obtain quantitative results for this increase in settling rate.

The effect of flow turbulence on particle settling rate is intimately related to the interaction of particles with local spatial structures of the flow. This interaction is represented by the notion of inertial bias (Maxey 1987) and best realized if one examines the instantaneous concentration field of particles. The inertial bias implies that the long-term particle concentration field may be quite non-uniform and local particle accumulation would occur. The local accumulation is evident for the cellular flow mentioned above and has been repeatedly observed for free shear flows such as plane mixing layer and jet flows (Crowe, Gore & Troutt 1985; Chung & Troutt 1988; Longmire & Eaton 1992; Lázaro & Lasheras 1992). One common feature of these relatively simple flows is that the scale governing the fluid velocity fluctuations is the same as the scale for the enstrophy or vorticity field. On the other hand, a range of flow scales co-exist in fully developed turbulence with integral scales governing the fluid velocity fluctuations, and smaller scales controlling the viscous dissipation and flow enstrophy field. This scale separation makes the problem of particle-turbulence interactions much more complicated. It is known that the large-scale turbulent motions determine the overall dispersion of particles (Reeks 1977; Squires & Eaton 1991*a*; Yeh & Lei 1991), however, the question of what flow scale should be used to characterize the local accumulation produced by inertial bias and the subsequent change in the particle settling remains open. The second objective of this study is to answer this question.

It is worth mentioning that some recent studies by She, Jackson & Orszag 1990, Brasseur & Lin 1991, and Ruetsch & Maxey 1991, 1992, have found that the more intense vorticity in a turbulent flow tends to form localized, coherent, and tube-like vortical structures at dissipation-range scales. This finding strongly suggests that the flow dynamics at small scales will play a significant role on the local particle accumulation, as it is most probably influenced by particle-flow vorticity interactions. Consequently, the flow dynamics at the dissipation range which is often viewed as of minor importance to particle dispersion must be correctly described when local accumulation and particle settling rate are considered. In this study, the method of direct numerical simulations (DNS) is similar to that used by Squires & Eaton (1991*a*) and is chosen to simulate the dynamical evolution of the turbulence. DNS is limited to

moderate flow Reynolds number because of resolution requirements and as such the range of scale separation in the flow is limited. Other methods such as large-eddy simulations (Yeh & Lei 1991) may allow for higher Reynolds numbers but are not adequate here since they do not provide the necessary details of flow dynamics at the smallest scales.

The paper is organized as follows. The main features of the isotropic, homogeneous, and stationary turbulent flows, simulated by solving the Navier–Stokes equations directly with a pseudospectral method, are presented in §2. Flow stationarity was achieved by forcing the low-wavenumber modes. For most of the simulations we adopted the forcing scheme of Eswaran & Pope (1988) and as used by Ruetsch & Maxey (1991, 1992). In one set of the simulations a different forcing scheme, based on a non-uniform force field (Hunt, Buell & Wray 1987), was employed as a comparison. This latter forcing scheme has been used to study the dispersion of heavy particles by Squires & Eaton (1991*a, b*). In §3 we describe the equation of motion for a heavy particle and the simulation methods used to obtain particle settling velocity and the concentration field. The results for a particle settling under the linear Stokes drag are reported first in §4. We will show that a significant increase in the mean settling velocity occurs when the particle inertial response time and the terminal velocity are made comparable to the flow Kolmogorov scales (§4.1). To explain such Kolmogorov scaling and the faster settling we then examine the particle concentration field and its correlations with flow vorticity and velocity fields (§4.2). A method for the direct quantification of local particle accumulation is introduced in §4.3 to reveal the significant role of small-scale flow dynamics. The effect of nonlinearity in the drag force is discussed in §5.

## 2. Turbulence simulation and flow characteristics

### 2.1. Flow simulation

The spectral code used to simulate the three-dimensional, unsteady flow in forced isotropic and homogeneous turbulence was originally developed by Ruetsch & Maxey (1991, 1992). A few modifications were made to improve the efficiency of the original code and to include the motion of the particles. Only a brief description of the simulation method is given here to provide the necessary information for the analysis of particle motion.

The Navier–Stokes equations governing the fluid motion are solved on a cube of side  $L = 2\pi$  using a pseudospectral method, with periodic boundary conditions applied in all three directions. This is a satisfactory approach provided that the integral lengthscale of the resulting flow is reasonably small compared to  $L$ . The flow cube is discretized uniformly into  $N^3$  grid points, which defines the wavenumber components in Fourier space as

$$k_j = \pm n_j(2\pi/L), \quad (2.1)$$

where  $n_j = 0, 1, \dots, \frac{1}{2}N$  for  $j = 1, 2, 3$ . A small portion of the energy at higher wave numbers,  $|k| \geq \frac{1}{2}N - 1.5$ , is truncated at each timestep to reduce aliasing errors, so the highest wavenumber realized in our simulation is  $k_{max} = \frac{1}{2}N - 1.5$ . It is clear that the grid resolution, the value of  $N$ , determines the ratio of the largest lengthscale of the turbulence to the smallest and thus the value of the flow Reynolds number. Four different grid resolutions were used in this study. Lower grid resolution simulations are relatively inexpensive to run and are good for a general parametric study of particle settling rate, but the different scales are not well separated. Higher grid resolution

Simulation grid	32 <sup>3</sup>	48 <sup>3</sup>	64 <sup>3</sup>	96 <sup>3</sup>	48 <sup>3*</sup>
$u'$	14.8	16.6	17.5	18.0	11.8
$L_f$	1.970	2.030	1.898	1.721	1.99
$\varepsilon$	2802	2943	3242	3620	970
$T_e$	0.078	0.083	0.091	0.098	0.145
$\lambda^\dagger$	0.8595	0.6525	0.5782	0.4739	0.871
$\eta$	0.0937	0.0617	0.0445	0.0293	0.0815
$\tau_k$	0.0146	0.0106	0.00831	0.00622	0.0189
$v_k$	6.41	5.83	5.36	4.73	4.30
$Re_\lambda$	21.2	31.0	42.5	61.5	30.0
$T_e/\tau_k$	5.3	7.8	11.0	15.8	7.7
$u'/v_k$	2.3	2.8	3.3	3.8	2.7
$\frac{\langle(\partial u/\partial x)^2\rangle}{\langle(\partial u/\partial x)^2\rangle^{\frac{3}{2}}}$	-0.407	-0.527	-0.501	-0.489	-0.541
$\frac{\langle(\partial u/\partial x)^4\rangle}{\langle(\partial u/\partial x)^2\rangle^2}$	3.68	3.94	4.06	4.46	4.27
$k_{max} \eta$	1.36	1.39	1.40	1.36	1.83
CFL	0.231	0.246	0.301	0.302	0.171
$\nu$	0.6000	0.3494	0.2381	0.1387	0.3494
$\delta t$	0.001‡	0.0003	0.000225	0.00015	0.0003

† Computed based on the dissipation,  $\lambda = (15\nu u'^2/\varepsilon)^{\frac{1}{2}} = (15)^{\frac{1}{2}}u'/\tau_k$ .

‡ It was reduced to 0.0005 for the computation of the settling rate of heavy particles with  $\tau_a = 0.005$ .

§ The flow was forced by a non-uniform force field on the modes of  $|\mathbf{k}| = \sqrt{2}$  with a forcing scale equal to 40 (see the appendix in Squires & Eaton 1991a).

TABLE 1. Flow parameters from the simulations

simulations are more time-consuming but provide a wider range of flow scales which is more representative of a naturally occurring turbulent flow. By varying the Reynolds number for a single class of homogeneous turbulent flow the effects of increasing scale separation on particle motion can be investigated.

The energy to maintain the flow is provided using a stationary, random forcing scheme developed by Eswaran & Pope (1988). In this forcing scheme an artificial forcing term is specified as a complex, vector-valued Uhlenbeck–Ornstein (UO) stochastic process. There are three parameters in the forcing scheme that affect the overall flow characteristics. The first is the forcing radius  $k_F$  which determines how many modes are subjected to the forcing. In our study, 80 modes defined by  $0 < |\mathbf{k}| < k_F = 8^{\frac{1}{2}}$  were forced. The mode  $\mathbf{k} = (0, 0, 0)$  represents a uniform mean flow and was set to zero at each timestep. To reduce the artifact from the forcing scheme on the large-scale motion, one would prefer a small forcing radius. However, the spatially averaged flow quantities show strong variations in time if the number of modes forced is too small. The above value of the forcing radius represents a compromise between these two considerations. The other two parameters are the forcing amplitude  $\sigma$  and timescale  $T_f$ , which specify the standard deviation and the correlation time of the UO process, respectively. These control the rate of energy addition (and thereby the dissipation rate) and the integral scales. These were fixed in the simulations at  $\sigma^2 = 447.3$  and  $T_f = 0.038$  as in Ruetsch & Maxey (1991, 1992). In addition to the grid resolution and forcing parameters, the only remaining physical parameter that needs to be specified for the flow simulations is the kinematic viscosity  $\nu$ . The velocity field

was started from rest and the flow was entirely generated from the forcing scheme and the nonlinear energy cascade. The spatial resolution of a spectral simulation is often monitored by the value of  $k_{max}\eta$ , which should be greater than one for the smallest scales of the flow to be resolved (Eswaran & Pope 1988), where  $\eta \equiv (\nu^3/\epsilon)^{\frac{1}{4}}$  is the Kolmogorov microscale. For the simulations in this study,  $k_{max}\eta$  was about 1.40. The Fourier coefficients of the flow velocity were advanced in time using a second-order Adams–Bashforth method for the nonlinear terms and a second-order Crank–Nicholson method for linear terms. The timestep was chosen to ensure that the CFL number was 0.3 or less for numerical stability and accuracy.

The forcing scheme for the low wavenumber range was used to generate a statistically stationary flow and avoid the complications presented by turbulence decaying in time. The stationary turbulence should also be representative of the dissipation range dynamics for locally isotropic turbulence, especially with the emphasis placed here on the resolution of Kolmogorov scales. As discussed by Ruetsch & Maxey (1992), forcing schemes of one form or another have been used by many investigators in the past, and, although one should be concerned about the artificial effects of forcing, these studies have all shown remarkably consistent results for the dynamics of the dissipation range. To provide a comparison with other forcing schemes, a second forcing scheme proposed by Hunt *et al.* (1987) and used by Squires & Eaton (1991*a, b*) was implemented for one set of the present simulations on a  $48^3$  grid. In this second scheme a non-uniform, time-independent, large-scale force field is added to the flow at each timestep. Non-zero forcing coefficients are applied only for the modes at  $|\mathbf{k}| = \sqrt{2}$  and their relative amplitudes are specified using the constraints of isotropy and incompressibility. Their final values are scaled in such a way that the resulting turbulence has about the same Reynolds number as the flow under the first forcing scheme for the same grid resolution. Originally we attempted to match the dissipation rate but the resulting integral scale under the second forcing scheme was too large compared to the box size  $L$ . Details of the forcing scheme are given in the appendix to Squires & Eaton (1991*a*).

## 2.2. Flow characteristics

In table 1 we list flow parameters for the simulations on various grid resolutions after the flow has become stationary (usually after two to three eddy turnover times). The quantities shown in the table (from top to bottom) are, the r.m.s. fluctuating velocity  $u'$ , the integral lengthscale for the longitudinal spatial velocity correlation  $L_f$ , the energy dissipation rate  $\epsilon$ , the eddy turnover time  $T_e \equiv u'^2/\epsilon$ , the transverse Taylor microscale  $\lambda$ , the Kolmogorov length ( $\eta$ ), time ( $\tau_k$ ), and velocity ( $v_k$ ) scales, and the Taylor microscale Reynolds number  $Re_\lambda = u'\lambda/\nu$ . The two ratios,  $T_e/\tau_k$  and  $u'/v_k$ , represent the maximum separation in the timescales and the velocity scales. In this study,  $T_e$  is defined using the outer lengthscale  $u'^3/\epsilon$  and the velocity scale  $u'$ , i.e.  $T_e = u'^2/\epsilon$ . It can be shown that for isotropic turbulence the scale separation is related to the Reynolds number as (Hinze 1975, p. 225)

$$T_e/\tau_k = Re_\lambda/15^{\frac{1}{2}} \approx Re_\lambda/3.9, \quad (2.2)$$

$$u'/v_k = Re_\lambda^{0.5}/15^{0.25} \approx Re_\lambda^{0.5}/2.0. \quad (2.3)$$

This indicates that the timescale separation tends to be larger than the velocity scale separation, which is consistent with the results in table 1. Also shown in table 1 are the velocity derivative skewness and flatness, the kinematic viscosity  $\nu$ , and the timestep size  $\delta t$ .

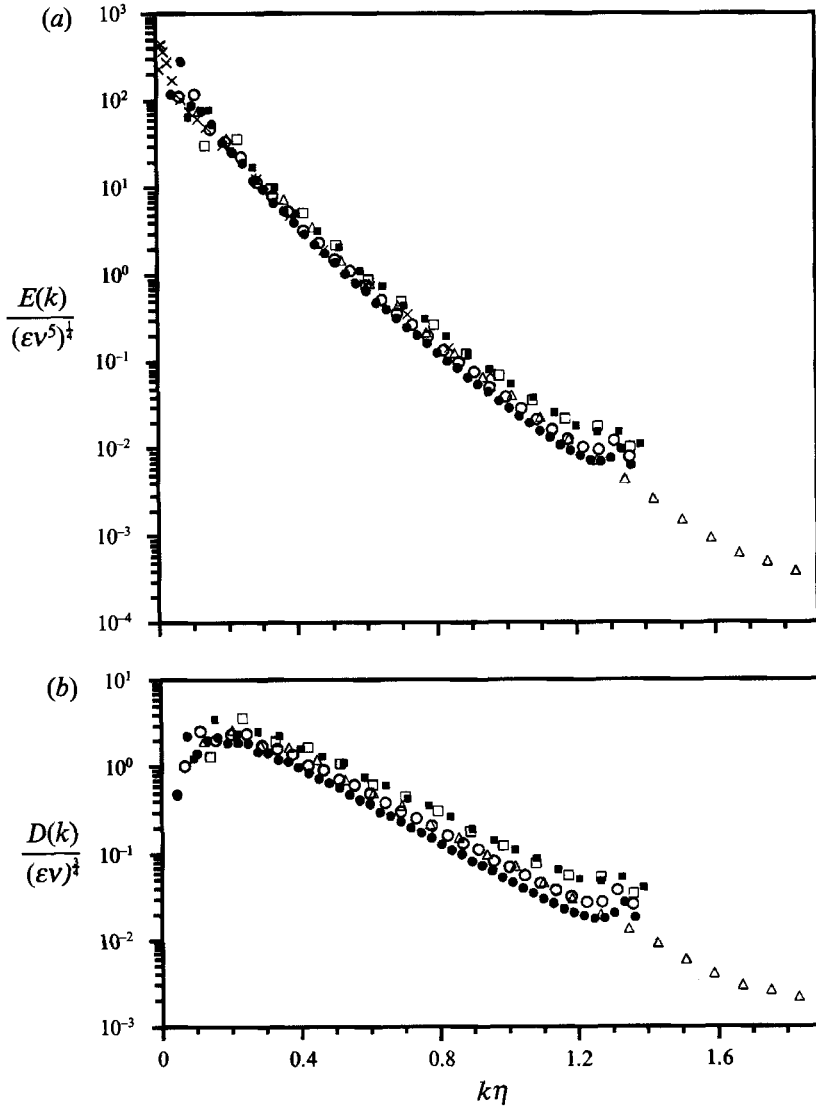


FIGURE 1. (a) The energy spectrum function  $E(k)$  for the simulated flows at various  $Re_\lambda$  using Kolmogorov scaling. The data taken from Comte-Bellot & Corrsin (1971) for a flow behind a 2-in grid at the location  $U_0 t/M = 98$  are plotted as a comparison; (b) dissipation spectrum function  $D(k)$ .  $\square$ ,  $32^3$ ,  $Re_\lambda = 21$ ;  $\blacksquare$ ,  $48^3$ ,  $Re_\lambda = 31$ ;  $\circ$ ,  $64^3$ ,  $Re_\lambda = 43$ ;  $\bullet$ ,  $96^3$ ,  $Re_\lambda = 62$ ;  $\triangle$ ,  $48^3$  and use of the second forcing scheme,  $Re_\lambda = 30$ ;  $\times$ , Comte-Bellot & Corrsin (1971),  $Re_\lambda \approx 65$ .

In figure 1 we present log-linear plots of the three-dimensional energy spectra for the simulations at different Reynolds numbers based on Kolmogorov scaling. The energy spectrum  $E(k)$  is defined in the standard manner such that

$$\frac{3}{2}u'^2 = \int E(k) dk. \quad (2.4)$$

The spectrum was calculated by dividing the wavenumber space into about  $\frac{1}{2}N$  shells according to the value of  $|k|$ , and then summing the kinetic energy in each shell. Also shown are a set of experimental data for the flow at  $U_0 t/M = 98$  downstream of a 2-

in grid taken from table 3 of Comte-Bellot & Corrsin (1971). Certain observations can be made from these results. First, the simulated energy spectra based on different grid resolutions and  $Re_\lambda$  show a reasonably good collapse for the Kolmogorov scaling, indicating a certain self-similarity of the dissipation-range flow dynamics. Secondly, the spectra compare very well with the experimental data, not only in terms of the general slope, but also the absolute values. One difference is that the data for the simulated spectra extend further below the dissipation length  $\eta$  (especially the one with the second forcing scheme) while the experimental data cover more of the large scales. Discrepancies between the simulations and experimental data are more significant at lower wavenumbers,  $k\eta < 0.1$ , when the spectra are plotted on a linear scale, as noted in Yeung & Pope (1989). The discrepancies are to be expected owing to the forcing but should not be a significant factor in the present study.

Also shown in figure 1 as a log-linear plot is the normalized spectrum for the dissipation of turbulent kinetic energy. The dissipation spectrum  $D(k)$  is related to  $E(k)$  by

$$D(k) = 2\nu k^2 E(k). \quad (2.5)$$

Domaradzki (1992) has proposed a physical model and scaling relations for energy transfer at high wavenumbers which leads to the conclusion that the energy spectrum  $E(k)$  should vary as  $E(k) \sim k^{-2} \exp(-ak)$  within the dissipation range. This would imply that  $D(k) \sim \exp(-ak)$  and indeed the present simulation results for  $D(k)$  do support this. The dissipation spectra as plotted follow nearly a straight line, though the collapse of the data for different Reynolds numbers is not as good as for the energy spectrum. Of importance here is the fact that the relative contribution of small scales (high wavenumbers) to the total dissipation is more significant than that to the total energy. This can be realized in two ways. First, there appears to be a peak in the dissipation spectra at  $k\eta \approx 0.2$ , though the energy spectra seems to decrease monotonically with  $k$ . The peak location for the dissipation spectra also compares reasonably well with the value of  $k\eta \approx 0.15$  observed in the measurements by Stewart & Townsend (1951) for grid-generated turbulence. Secondly, at large  $k$  the rate at which  $D(k)$  decreases is smaller than for the energy spectrum  $E(k)$ , by a factor of  $k^2$  by definition. We note that the enstrophy spectrum for homogeneous isotropic turbulence is proportional to the dissipation spectrum. Therefore, small scales play a much more significant role in the vorticity fluctuations than in the velocity fluctuations even before one considers the intermittent nature of the more intense vorticity fluctuations.

The one-dimensional energy spectra are often directly measured for grid-generated turbulence (Comte-Bellot & Corrsin 1971; Snyder & Lumley 1971; Wells & Stock 1983). These can also be more accurately computed than the three-dimensional spectra in the simulations since the modes are more evenly distributed and an average over the three different directions can be performed. The one-dimensional energy spectrum  $E_{11}(k_1)$  is defined as

$$u'^2 = \int E_{11}(k_1) dk_1. \quad (2.6)$$

In figure 2 we display the normalized one-dimensional energy spectra. A very good collapse of data is seen on the log-log plots. The line in figure 2 is a curvefit to the experimental data of Comte-Bellot & Corrsin (1971) for their 2-in grid case. The curvefit is shown here since the experimental data at different downstream locations collapse when plotted under Kolmogorov scaling. Further, the spectrum curve for their 1-in grid case is very much the same as that for  $k\eta \geq 0.01$ . We also made a comparison of Comte-Bellot & Corrsin's spectrum data with those of Snyder & Lumley (1971) and



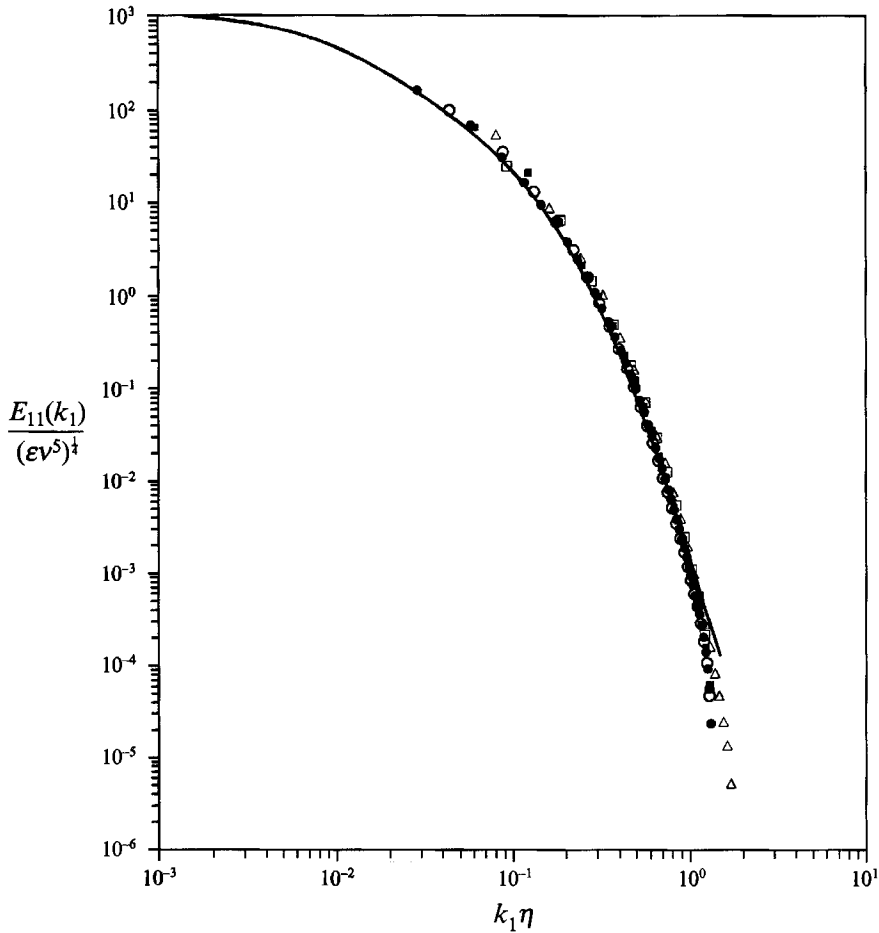


FIGURE 2. The one-dimensional energy spectra for the simulated flows at various  $Re_\lambda$  under Kolmogorov scaling:  $\square$ ,  $32^3$ ,  $Re_\lambda = 21$ ;  $\blacksquare$ ,  $48^3$ ,  $Re_\lambda = 31$ ;  $\circ$ ,  $64^3$ ,  $Re_\lambda = 43$ ;  $\bullet$ ,  $96^3$ ,  $Re_\lambda = 62$ ;  $\triangle$ ,  $48^3$  and use of the second forcing scheme,  $Re_\lambda = 30$ . The line is a curvefit for all the measured data taken from Comte-Bellot & Corrsin (1971) for a flow behind a 2-in grid.

Wells & Stock (1983), both of which studied the dispersion of heavy particles in a grid-generated turbulence, and found that all the experimental curves agree very well for  $k\eta \geq 0.01$ . Such universality of the energy spectrum is reproduced by the simulations, although this is somewhat surprising as the flow Reynolds numbers are not high. The flow Reynolds numbers for all the above experimental measurements are comparable to those in our simulations. As a side note, George (1992) recently suggested a different scaling using  $\lambda$  and  $u'$  for the energy spectrum rather than Kolmogorov scaling for self-preserving decaying turbulence. For our forced stationary turbulence, we found, however, the Kolmogorov scaling collapses data much better than the suggested Taylor scaling.

Finally, the velocity derivative skewness and flatness are shown in table 1. The velocity derivative skewness in our simulations is in the range  $-0.55$  to  $-0.40$ , which compares very well with the experimental range  $-0.5$  to  $-0.3$  for  $Re_\lambda < 100$  (Van Atta & Antonia 1980). The flatness also agrees with the experimental value of about 4. In summary, although the simulated flows are contaminated by the artificial forcing and

have only low to moderate Reynolds numbers (thus there is no discernible inertial subrange), they do, at least, compare very well with experiments for grid-generated turbulence and appear to represent realistically the dissipation-range dynamics.

### 3. Simulation method for heavy particles

#### 3.1. Equation of particle motion

We consider the motion of heavy spherical particles in a uniform, isotropic, stationary, and homogeneous turbulent flow. The particle is assumed to be small in comparison with the Kolmogorov microscale of the turbulence and the loading dilute enough that the presence of the particles does not modify the turbulence structure. On the other hand, the particle is considered to be much larger than the molecular mean free path (Clift, Grace & Weber 1978, p. 272) and to have an aerodynamic response time much larger than the mean molecular collision time so that the effect of Brownian motion can be neglected in comparison to the dispersion by turbulent eddies. Since in grid-generated turbulent flow of air (Snyder & Lumley 1971) the Kolmogorov microscale is typically in the range 300 ~ 700  $\mu\text{m}$  and in atmospheric turbulence of 1 mm, the above assumptions are applicable to the dispersion of particles in the size range 10 ~ 200  $\mu\text{m}$ .

Under the assumption that the density of the particle  $\rho_p$  is much larger than the density of the fluid  $\rho_f$ , (say,  $\rho_p/\rho_f \geq 100$ ) the BBO (Basset–Boussinesq–Oseen) equation of motion (Maxey & Riley 1983) reduces to the following form

$$\frac{dV(t)}{dt} = \frac{(\mathbf{u}(Y, t) - V(t))f(Re_p) + \mathbf{W}}{\tau_a}, \quad (3.1)$$

$$\frac{dY(t)}{dt} = V(t), \quad (3.2)$$

where  $V(t)$  and  $Y(t)$  are the velocity and the centre position of a heavy particle, respectively;  $\mathbf{u}$  is the fluid velocity field. The Stokes response time is  $\tau_a$  and  $\mathbf{W}$  is the Stokes terminal velocity,

$$\tau_a = \frac{\rho_p d_p^2}{18\mu}, \quad \mathbf{W} = \tau_a \mathbf{g}; \quad (3.3)$$

where  $d_p$  is the diameter of the particle,  $\mu$  is the dynamic viscosity of the fluid, and  $\mathbf{g}$  is the acceleration due to gravity. The magnitude of the terminal velocity,  $|\mathbf{W}|$ , will be denoted by  $W$ .

We start by assuming the drag force acting on a particle as it moves through the flow is a linear Stokes drag, so that the coefficient  $f(Re_p)$  in (3.1) is set to 1. A Stokes drag law is only valid when the particle Reynolds number,  $Re_p = d_p |V - \mathbf{u}|/\nu$ , is much less than one. However, owing to the finite drift velocity, the particle Reynolds number may often be of the order of one for larger particles. In general an appropriate nonlinear drag should be used when considering such particles. One approach would be to include a quasi-steady drag force where the coefficient  $f(Re_p)$  is determined by the instantaneous value of the particle Reynolds number. This is explored further in §5, but for the present a Stokes drag law will be assumed.

When the Stokes drag is used, the two particle parameters defined in (3.3) describe a timescale (or inversely a response frequency) and a velocity scale. On the other hand, for a turbulent flow there is no single set of scales but rather a continuous spectrum of

time and velocity scales. The larger scale, more energetic motions may be characterized by the r.m.s. fluid velocity  $u'$  and the integral lengthscale  $L_f$ ; while the smaller scale, dissipative motions may be characterized in terms of the Kolmogorov microscales. As pointed out in §1, the values of the particle parameters have to be chosen relative to the scales of the fluid motion if any effect of the flow on the settling rate is to be observed. Their values should also be consistent with the assumptions made in deriving the equation of motion. It can be shown that

$$\frac{\tau_a}{\tau_k} = O\left(\frac{\rho_p}{\rho_f} \frac{d_p^2}{\eta^2}\right); \quad \frac{W}{v_k} = O\left(\frac{\rho_p d_p^2 g}{\rho_f \eta^2 v_k \tau_k}\right). \quad (3.4)$$

We are mainly interested in the parameter range where both  $\tau_a/\tau_k$  and  $W/v_k$  are of the order of one, for which a substantial change in the particle settling rate will be observed. This parameter range is realizable as long as the density ratio is made large enough. The particle Reynolds number may be written as

$$Re_p = O\left(\frac{d_p \max(u', W)}{\eta v_k}\right), \quad (3.5)$$

which can be made small if  $d_p/\eta \ll 1$ .

### 3.2. Mean settling rate: a triplex averaging procedure

In this section, we present the method for settling velocity computation. Previous experience with random flow fields (Maxey 1987) indicates that the relative change in particle settling rate is usually small, so a reliable method that can calculate the average settling rate accurately with small statistical error is necessary for one to capture such small changes. For this purpose, we developed a triplex averaging procedure to compute the mean settling rate.

The first step of the simulations was to obtain a statistically stationary flow velocity field, during which no particles were introduced. This velocity field was then saved as a starting flow field for the study of particle settling, i.e. it was repeatedly used for different sets of particle parameters.

The second step was to introduce particles into the flow. The particles were divided into six groups of different orientations for the gravity. The six orientations,  $\mathbf{g}/|\mathbf{g}|$ , are  $(1, 0, 0)$ ,  $(-1, 0, 0)$ ,  $(0, 1, 0)$ ,  $(0, -1, 0)$ ,  $(0, 0, 1)$  and  $(0, 0, -1)$ . We denote these six unit vectors by  $\mathbf{e}^{(\beta)}$  with  $\beta = 1, 2, \dots, 6$ . Each group contained  $N_p = 4096$  particles which were located randomly with uniform distribution in the computation box at the time they were released. The initial velocity for each particle was assumed to be the terminal velocity  $W$ . This choice of the particle initial velocity is arbitrary but should have no influence on the long-time particle settling rate.

The third step was to advance the flow and the motion of particles simultaneously. The total computation time for this last step was respectively about 46, 12, 8 or 5 times the eddy turnover time  $T_e$  for the different flow grid resolutions, from the lowest ( $32^3$ ) to the highest ( $96^3$ ). The trajectory of an individual particle was obtained by numerical integration of the equation of motion using a fourth-order Adams–Bashforth method for the particle velocity and a fourth-order Adams–Moulton method for the particle location. In many cases, it was found that even a second-order Adams method resulted in the same particle trajectory over a long period of time. The timestep was the same as that used for flow advancement. Since the particle position usually does not coincide with the grid points for the flow simulations, the fluid velocity at the location of the particle is derived using a partial-Hermite interpolation scheme introduced by

Balachandar & Maxey (1989). If the particle moves out of the simulation box, the flow velocity field is extended periodically in all directions to allow the interpolation of fluid velocity at any spatial point. At each timestep of the integration, the change in the settling rate relative to the terminal velocity averaged over the 4096 particles for each group,

$$\Delta V_i^{(\beta)} \equiv \overline{[(V_i - W_i)]^{(\beta)}} \quad (i = 1, 2, 3), \quad (3.6)$$

was computed, where the overbar denotes this first averaging. In addition, the r.m.s. particle fluctuating velocity,

$$\sigma_i^{(\beta)} \equiv \overline{[(V_i - \bar{V}_i)^2]^{1/2}(\beta)} = \overline{[(V_i - \bar{W}_i)^2 - (\Delta V_i)^2]^{1/2}(\beta)}, \quad (3.7)$$

and r.m.s. relative velocity between a particle and the nearby fluid,

$$\theta_i^{(\beta)} \equiv \overline{[(V_i - \bar{W}_i - u_i(\mathbf{Y}, t))^2]^{1/2}(\beta)}, \quad (3.8)$$

were calculated. It should be noted that the mean value of the relative fluctuation velocity,  $(V_i - \bar{W}_i - u_i(\mathbf{Y}, t))$ , is zero after the initial transient. Further  $\theta_i^{(\beta)}$  approaches zero when  $\tau_a/\tau_k \rightarrow 0$ .

To obtain an idea of how the particle motion approaches a stationary state from the arbitrary initial conditions, we now examine the mean quantities after the above first averaging for a typical simulation with  $\tau_a/\tau_k \approx 1.0$  and  $W/v_k \approx 1.0$  on the  $96^3$  grid. These results are presented in figure 3, where  $t = 0$  corresponds to the time at which the particles are released. Several observations can be made here. The transient time for the mean settling rate to reach a stationary state is about 0.09, which is close to the value of large-scale eddy turnover time  $T_e$  of 0.098 (see table 1). In general this transient time was found to be quite independent of the particle response time for the values of  $\tau_a$  studied and in all cases  $\tau_a$  was much smaller than  $T_e$ . In addition the mean settling rate after the transient interval oscillates in time on a timescale of the order  $T_e$ . These indicate the settling rate is influenced by large-scale turbulent motion although the particle response time is on the order of the Kolmogorov scale. The statistical variation in the settling rate after the first averaging and after the initial transient stage should be of the order of  $\sigma_i^{(\beta)}/(N_p)^{1/2}$ . For some initial tests,  $N_p$  was taken to be 1024 and we found the fluctuation amplitude was indeed twice as large. It should also be noted that the final results may not be necessarily better if  $N_p$  is made much larger since only a limited number of flow scales, particularly large scales, are involved in the simulated flow at a given time. To remedy this defect of the simulated flows, we chose to continue the simulations for a longer time interval with a moderate number of particles and to use a time-average. It may also be seen from figure 3 that  $\Delta V_1^{(1)}$  is positive and the other two components are close to zero. Therefore, on average a particle settles in the direction of the gravity with a greater mean velocity than the terminal velocity. The transient time for the r.m.s. particle velocity is much shorter and was found to depend on the particle response time, i.e. about  $4\tau_a$ . The transient time for the r.m.s. relative velocity is the shortest and was found to be about  $2 \sim 3\tau_a$ . There also appears to be a slight overshoot at the end of the transient interval, which was found to be more pronounced as the particle response time was increased. Unlike the settling rate and the r.m.s. particle velocity, the particle-averaged magnitude of the relative velocity shows much less statistical variation at any instant. This is consistent with the smaller scale turbulent motions dominating the relative velocity, since at any instant there are many more of these than the larger eddies within the computation domain.

The final step was to perform two further averaging processes, namely over time and over orientation. After averaging over particles for each group, we can obtain better

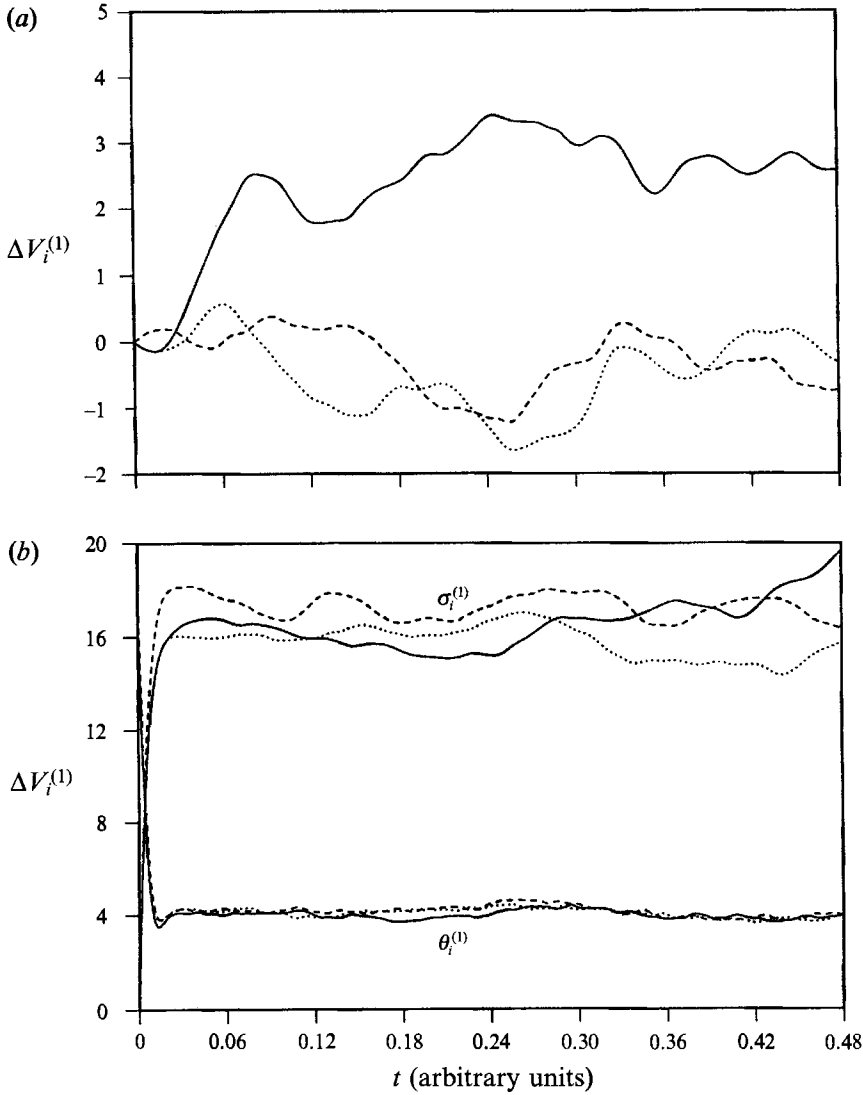


FIGURE 3. The particle velocity statistics in arbitrary units after the first averaging for  $\beta = 1$  where the gravity is oriented in the  $+x_1$  direction. The mesh size is  $96^3$ ,  $Re_\lambda = 62$ , and particle parameters are  $\tau_a = \tau_k$ ,  $W = v_k$ . —,  $x_1$ -component ( $i = 1$ );  $\cdots$ ,  $x_2$ -component ( $i = 2$ ); ---,  $x_3$ -component ( $i = 3$ ). (a) the mean velocity  $\Delta V_i^{(1)}$ ; (b) the r.m.s. particle velocity  $\sigma_i^{(1)}$  and the r.m.s. relative velocity  $\theta_i^{(1)}$ .

results by averaging over the six orientations of gravitational settling. For example the relative increase in the settling rate in the direction of gravity is

$$\Delta V_1 \equiv \frac{1}{6} \sum_{\beta=1}^6 \Delta V^{(\beta)} \cdot e^{(\beta)}, \quad (3.9)$$

and orthogonal to the direction of gravity it may be averaged as

$$\Delta V_2 \equiv \frac{1}{12} (\Delta V_2^{(1)} + \Delta V_3^{(1)} + \Delta V_2^{(2)} + \Delta V_3^{(2)} + \Delta V_1^{(3)} + \Delta V_3^{(3)} + \Delta V_1^{(4)} + \Delta V_3^{(4)} + \Delta V_1^{(5)} + \Delta V_2^{(5)} + \Delta V_1^{(6)} + \Delta V_2^{(6)}), \quad (3.10)$$

where it is assumed that there is no statistical difference between the two horizontal

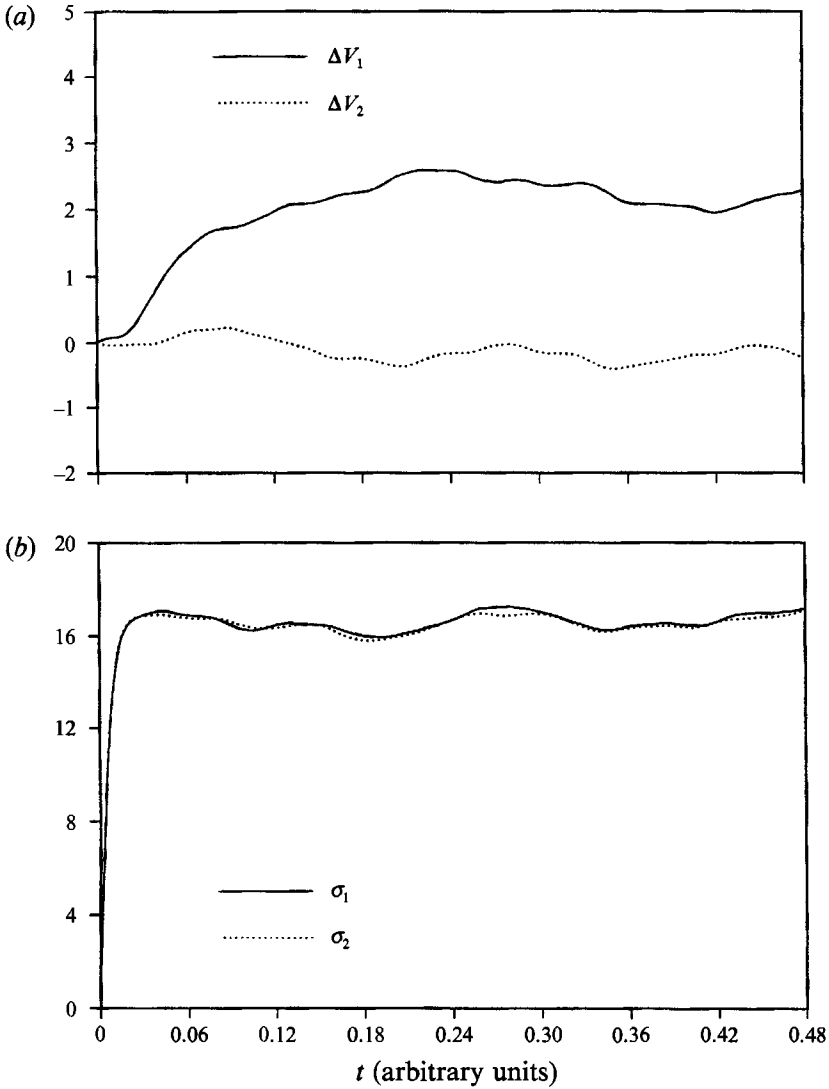


FIGURE 4. The particle velocity statistics in arbitrary units after the second averaging as a function of time: (a) the mean velocity  $\Delta V_i$ ; (b) the r.m.s. particle velocity  $\sigma_i$ . The mesh size is  $96^3$ ,  $Re_\lambda = 62$ , and particle parameters are  $\tau_a = \tau_k$ ,  $W = v_k$ .

directions for each group owing to symmetry considerations. Similar averaging can be performed to obtain the r.m.s. particle velocity and relative velocity, and these results are denoted by  $\sigma_1$ ,  $\sigma_2$ ,  $\theta_1$  and  $\theta_2$ . This second averaging process cancels the effect of any directional bias (anisotropic features) that may exist for a single realization of the simulated flow. Figure 4 shows the results after the second averaging for the same particle parameters as in figure 3. We see that the fluctuations are greatly reduced. Finally we average the settling rate over time starting at  $t = 2T_e$ ,

$$\langle \Delta V_1 \rangle \equiv \frac{1}{(m-2)T_e} \int_{t=2T_e}^{t=mT_e} \Delta V_1(t) dt, \quad (3.11)$$

where  $mT_e$  is the total integration time for the motion of particles. This third averaging

process can be applied to other quantities and the final results will be denoted with angle brackets. The standard deviation on  $\langle \Delta V_1 \rangle$  can be approximated by  $\langle \sigma_1 \rangle / [3N_p(m-2)]^{1/2}$  (Bendat & Piersol 1971) if  $(m-2)$  is much larger than one and the correlation time for  $\Delta V_1$  is assumed to be of the order of  $T_e$ . This last averaging process is equivalent to the ensemble averaging over a different realization of the flow. For the case shown in figure 4, the triplex averaging procedure results in  $\langle \Delta V_1 \rangle = 2.23 \pm 0.09$ . This may be compared with the value of  $W$  here equal to  $v_k = 4.73$ . The first and the third averaging processes can be replaced by recording the change in the mean particle location for each group between the end of the integration and  $t = 2T_e$  and dividing the result by the time interval. This alternative way has also been used in the code and shown to result in the same average settling rate.

The code was optimized and run on a CRAY Y-MP. For the  $32^3$  grid resolution case and the number of particles involved, the CPU time was 0.12 s for the flow evolution and 0.78 s for the tracking of all the particles at each timestep when the code was run on a single processor. While for the  $96^3$  case, the CPU time was 2.2 s for the flow evolution and 2.8 s for the tracking of the particles at each timestep. Therefore 87% of the CPU time was used for moving the particles at the lowest resolution and 56% at the highest resolution. The required CPU time for a complete run was about one hour on  $32^3$  grid and five hours on  $96^3$ . For the production runs, the code was parallelized to make use of more than one processor (normally three) to reduce the turnaround time and the charges for memory use.

### 3.3. Simulation of concentration distribution

While in the settling velocity computation efforts are made to reduce the final statistical error, the aim in the simulation of concentration distribution is to obtain a reasonable visual representation of the instantaneous spatial distribution of the particle locations. This is achieved with the use of a much larger number of particles, but owing to the limitations on available computer resources, the concentration is simulated only for a  $48^3$ -grid. 131072 particles were used with a single orientation of the gravity parallel to the  $x_1$ -axis. Initially, the particles were placed randomly in the box with a uniform distribution in their locations. The initial velocity is set to the terminal velocity for each particle. The concentration,  $C$  at any grid point is defined here as the number of particles found inside a small cube with its centre at the grid point and its side equal to the grid spacing. This number and hence the concentration  $C$  may take a value of zero or a positive integer. We note that a constant factor might be introduced to our present definition of concentration to give other definitions, but it does not affect the subsequent discussions and results of this study. The grid spacing is about twice the Kolmogorov scale  $\eta$  so that variations of the concentration field at a scale below  $2\eta$  will not be resolved. Fortunately, the lengthscale associated with regions of intense vorticity is about  $6\eta$  or larger (Ruetsch & Maxey 1991). Thus this definition of concentration is capable of revealing satisfactorily the particle-vorticity field correlations. If a particle leaves the computation box, its periodic image can be used to preserve the total number in the box. Therefore as the total number of particles is constant and the turbulence homogeneous the mean particle concentration at any point is constant. As defined here, this uniform, mean concentration,  $\langle C \rangle$  is  $131072/48^3$  or 1.185. In any single simulation of the turbulence the initially non-coherent, statistically uniform, particle concentration will evolve to a coherent distribution as a result of dynamical interaction with the turbulence.

This dynamical interaction is best seen in the transient interval when the initial, uniform concentration distribution responds to the evolving turbulence and quickly

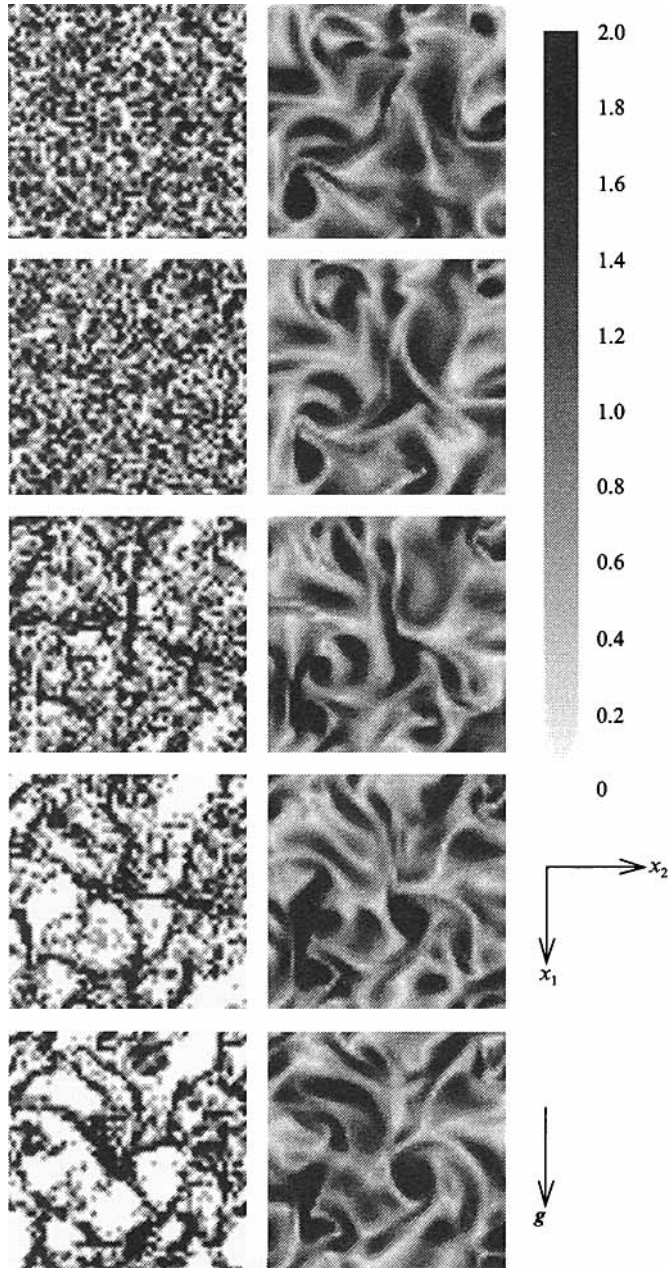


FIGURE 5. Normalized particle concentration (left-hand side) and flow scalar-vorticity field (right-hand side) on an  $(x_1, x_2)$ -slice ( $x_3 = 27L/48$ ) at the 5 consecutive time frames. The first frame is at  $t = 0$  when the concentration is uniform. The time interval is 0.018 or about twice the Kolmogorov timescale. The mesh size is  $48^3$ ,  $Re_\lambda = 31$ , and particle parameters are  $\tau_a = \tau_k$ ,  $W = v_k$ .

becomes non-uniform as time increases. We present in figure 5 the evolution of a typical normalized concentration field,  $C/\langle C \rangle$ , and the scalar-vorticity field on a slice from the three-dimensional simulation box at five consecutive time frames during the initial development period. The normalized scalar-vorticity  $\Omega$  is defined as  $(\omega_i \omega_i)^{\frac{1}{2}} / \langle (\omega_i \omega_i)^{\frac{1}{2}} \rangle$ , where  $\omega_i$  is the flow vorticity. Throughout this paper, the grey scale is



defined such that black denotes at least twice the corresponding field mean and white represents a zero local value. Since  $C$  can only take discrete integers and its mean is 1.1852, the four grey levels appearing in the concentration field denote a local concentration of  $C = 0, 1, 2$  and  $\geq 3$ , respectively.

For the purpose of quantification, we now introduce two probability functions for the concentration field. The first is the probability of finding the concentration at a grid point equal to a particular value  $C$ , denoted by  $P_c(C, t)$ . This first probability function was also used in the work of Squires & Eaton (1991*b*). A second probability,  $P_n(C, t)$ , is defined by the percentage of the particles (out of 131072) that are found at those grid points where the concentration is at a given value  $C$ .  $P_n(C, t)$  represents the relative importance of a specific particle concentration in accounting for the total number of particles. Obviously the two probability functions are related by

$$P_n(C, t) = \frac{N_g}{N_p} P_c(C, t) C = 0.84375 P_c(C, t) C, \quad (3.12)$$

where  $N_g = 48^3$  is the number of grid points and  $N_p = 131072$  is the number of particles followed in the simulation. For the uniform concentration field at  $t = 0$ , the probability  $P_c$  can be found exactly, i.e.

$$P_c(C, t = 0) \equiv P_c^u(C) = \binom{N_p}{C} \left(\frac{1}{N_g}\right)^C \left(1 - \frac{1}{N_g}\right)^{N_p - C} \quad \text{for } C = 0, 1, 2, \dots, N_p, \quad (3.13)$$

where

$$\binom{N_p}{C} = \frac{N_p(N_p - 1) \dots (N_p - C + 1)}{C!}. \quad (3.14)$$

It follows then the probability for each of the four levels in the concentration field at  $t = 0$  is

$$\left. \begin{aligned} P_c^u(C = 0) &= 0.3057, & P_c^u(C = 1) &= 0.3623, \\ P_n^u(C = 2) &= 0.2147, & P_n^u(C \geq 3) &= 0.1173. \end{aligned} \right\} \quad (3.15)$$

The relative proportion of the four differently shaded regions changes with time. The fact that particles tend to accumulate in the low-vorticity region (Maxey 1987) implies that the probability for the void region in the concentration field where  $C = 0$  or region of white should increase with time during the transient period, as shown in figure 6. It is also seen that the probability for the black region increases with time, and that for the other intermediate concentrations decreases. Interestingly, the relative proportion changes rather slowly for  $t < 0.02$  which may be an effect of initial condition for the particle velocity. The main changes seem to occur for  $0.02 < t < 0.1$  and the concentration field approaches a statistically stationary state for  $t > 0.1$ . This transient time appears to be the same as that for the mean settling rate, i.e. both are of the order of the eddy turnover time. Further analysis of local accumulation and correlation between the concentration and flow vorticity field is presented in the next section, where we will focus on the particle motion at the statistically stationary state.

#### 4. Results and analysis

In this section we first present the results on mean settling rate and other statistics for various particle parameters and grid resolutions. Particle concentration fields are then examined for the mechanism responsible for the change in the settling rate. We

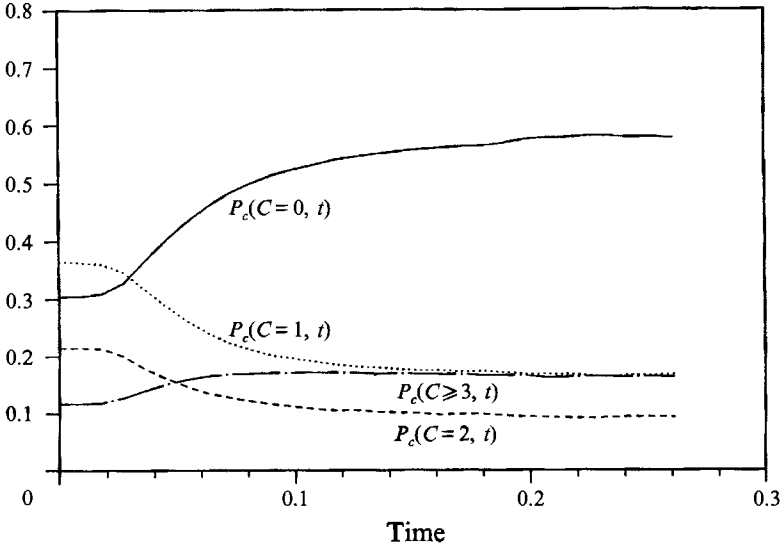


FIGURE 6. The transient behaviour of the concentration probabilities for  $\tau_a/\tau_k = W/v_k = 1$  on  $48^3$  grid,  $Re_\lambda = 31$ .

intend to answer the following questions: when does the maximum change in the settling rate occur, how is the relative change related to the inertial bias and local accumulation, and what are the respective roles of different flow scales?

#### 4.1. Settling rate for heavy particles

Initial tests showed that the most significant change in the long-time mean settling rate occurs when the particle response time  $\tau_a$  and the terminal velocity  $W \equiv |W|$  are made comparable to flow Kolmogorov scales. Therefore we shall focus on this parameter range. Figure 7 shows the increase in mean settling velocity  $\langle \Delta V_1 \rangle / v_k$  as a function of  $\tau_a/\tau_k$  for a fixed relative terminal velocity,  $W/v_k = 1.0$ , on various grid resolutions as listed in table 1. It may be seen that  $\langle \Delta V_1 \rangle / v_k$  is always positive. It increases with  $\tau_a$  if  $\tau_a/\tau_k$  is less than 0.5 and reaches a maximum when  $0.5 < \tau_a/\tau_k < 1$ . It then decreases with  $\tau_a$  and approaches to zero as  $\tau_a/\tau_k$  becomes much larger than one, though  $\tau_a$  may still be less than  $T_e$ . This qualitative feature is robust and does not appear to change with the flow Reynolds number. Similar results were obtained by Maxey (1987) for particles settling in random flow fields. As mentioned earlier these random flows, which were generated in terms of random Fourier modes that satisfied constraints for incompressible flow, had no coherent dynamics and the energy spectrum was quite narrowly centred around a single, large-eddy scale. In that study the largest increase in the average settling velocity was found to occur when  $\tau_a$  was about  $0.2L_f/u'$ , or equivalently for the data here when  $\tau_a/T_e$  was about  $\frac{1}{4}$ . The limited range of scales in the earlier study meant that there was no distinguishable dissipation range, or meaningful distinction between  $T_e$  and  $\tau_k$ . The measured increases in the average settling velocity are also significantly greater in the present study. Here the largest increase  $\langle \Delta V_1 \rangle$  observed is 27% of the terminal velocity for simulations on the  $32^3$ -grid and 45% on the  $96^3$ -grid, from the data in figure 7. The increase in settling velocity when scaled by the Kolmogorov velocity is larger for higher values of  $Re_\lambda$ , within the first group of simulations. The alternative forcing scheme, based on the methods of Squires & Eaton (1991a), shows an even larger increase in the settling velocity. The

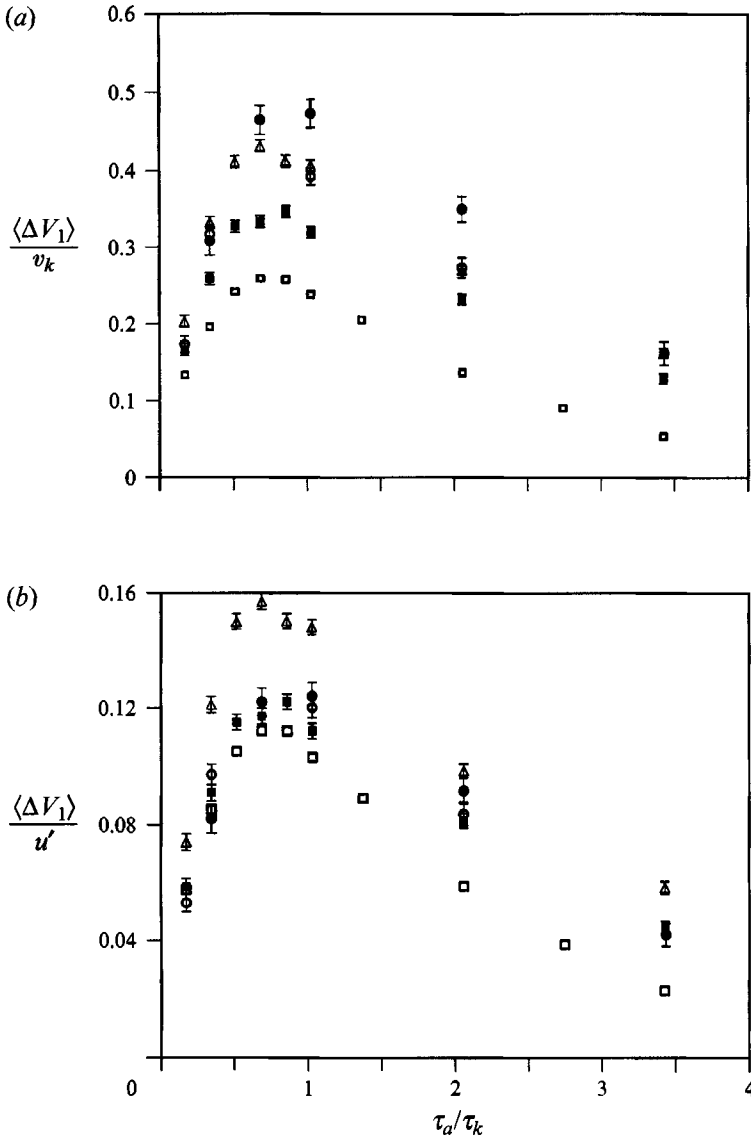


FIGURE 7. The increase ( $\langle \Delta V_1 \rangle$ ) in the particle mean settling velocity as a function of  $\tau_a / \tau_k$  for a fixed terminal velocity,  $W = v_k$ . The error bar represents the statistical uncertainty. (a) Normalized by Kolmogorov velocity scale  $v_k$ ; (b) normalized by r.m.s. fluid velocity  $u'$ .  $\square$ , 32<sup>3</sup>,  $Re_\lambda = 21$ ;  $\blacksquare$ , 48<sup>3</sup>,  $Re_\lambda = 31$ ;  $\circ$ , 64<sup>3</sup>,  $Re_\lambda = 43$ ;  $\bullet$ , 96<sup>3</sup>,  $Re_\lambda = 62$ ;  $\triangle$ , 48<sup>3</sup> and use of the second forcing scheme,  $Re_\lambda = 30$ . For the 32<sup>3</sup> simulations, the size of the symbol is made the same as the error bar.

value of  $\tau_a / \tau_k$  at which  $\langle \Delta V_1 \rangle / v_k$  is greatest is consistently within the interval of  $0.5 < \tau_a / \tau_k < 1$  and is centred around 0.8 as the Reynolds number  $Re_\lambda$  is varied. By contrast, the ratio of  $T_e / \tau_k$  varies from 5.3 to 15.8, so that if the data were presented in terms of the ratio of  $\tau_a$  to  $T_e$ , which is also representative of Lagrangian integral timescales, then there would be a much greater variation in the location of the peak increase with changing  $Re_\lambda$ .

These results are also shown in figure 7 where  $\langle \Delta V_1 \rangle$  is normalized by  $u'$ . We see that the quantitative difference among the simulated results for different  $Re_\lambda$  with the first

forcing scheme is greatly reduced. Therefore we may conclude that while the qualitative dependence of  $\langle \Delta V_1 \rangle$  on  $\tau_a$  follows Kolmogorov scaling, the quantitative value is still affected by large-scale fluid motion. This is partly related to the fact that the flow field has a limited scale separation and the fact that the change in particle settling velocity will be affected by a range of flow scales in the neighbourhood of its response time, as mentioned in §1. More specifically variations in the local fluid velocity in the neighbourhood of the particle that occur on a timescale much shorter than  $\tau_a$  will produce no response in the particle motion and make no contribution to the average settling velocity. Variations that occur on a very slow timescale compared to  $\tau_a$  will lead to a perfect response in the particle motion with no relative velocity induced by the inertia of the particle. Of importance is how the interval of timescales centred on  $\tau_a$  compares to  $T_e$  and  $\tau_k$ . Another factor is that the low-vorticity region where particles tend to accumulate often resembles the large-scale flow features, as will be shown later. The value  $\langle \Delta V_1 \rangle / u'$  increases with the flow Reynolds number for most  $\tau_a$ , indicating that for most cases the range of scales to which the particles can respond is wider than the scale separation covered by the simulations. However, when  $\tau_a$  is very small such that  $\tau_a / T_e \ll 1$ , the particles can respond to the large-scale flow exactly. In this case the large-scale flow will not affect the settling rate. This implies that the value  $\langle \Delta V_1 \rangle / u'$ , at a given small value of  $\tau_a / \tau_k$ , for higher  $Re_\lambda$  can be less than that for a lower  $Re_\lambda$  case. This reversion is observed at  $\tau_a / \tau_k = 0.34$  where  $\langle \Delta V_1 \rangle / u' = 0.082 \pm 0.005$  on the  $96^3$ -grid while  $\langle \Delta V_1 \rangle / u' = 0.097 \pm 0.004$  on the  $64^3$ -grid. We can claim that at  $\tau_a = 0.34\tau_k = 0.002$  the largest scales of the  $96^3$  flow ( $T_e = 0.098$ ,  $T_e / \tau_a = 49$ ) have no effect on the settling. Other evidence of the reversion may be seen at  $\tau_a / \tau_k = 0.17$  on the  $64^3$ -grid as compared to the lower grid resolutions. This reversion should have been observed for all the  $\tau_a / \tau_k$  of the order of one, where the most substantial change in the settling occurs, had the simulations been performed at a sufficiently high  $Re_\lambda$  such that  $T_e / \tau_k \gg 1$ . The reduced influence of the large scales on the mean settling rate also implies a reduced influence from the artifacts of the flow forcing on the particle settling rate. This, then, would lead one to expect similar results to hold for even higher Reynolds number flows, which at present we are unable to simulate. For example, in atmospheric turbulence where the flow scales are widely separated, the mean settling rate of small particles would only be affected by a limited range of flow scales near the dissipation range, the settling rate should be expected to be much larger than the terminal velocity as indicated by the present results. Both the growth rate of water droplets in clouds and the residence time of dust or aerosols in the atmosphere will be influenced by such changes in the settling rates (Pruppacher & Klett 1978).

Next the changes in the settling velocity with changes in the terminal fall velocity are considered. Figure 8 shows  $\langle \Delta V_1 \rangle / v_k$  as a function of terminal velocity for a fixed value of the relative inertia,  $\tau_a / \tau_k = 1.0$ . Initially the ratio  $\langle \Delta V_1 \rangle / v_k$  increases rapidly as the terminal velocity  $W / v_k$  varies between 0 and 1 for a particular Reynolds number. The increase then begins to level off and  $\langle \Delta V_1 \rangle / v_k$  reaches a maximum somewhere in the interval  $1.5 < W / v_k < 2.5$ , before decreasing at higher values of the terminal velocity. The location of the maximum, at least for the first set of simulations, tends to occur at higher value of  $W / v_k$  as the Reynolds number is increased. These qualitative features are similar to those of figure 7. This may be expected since an increase in  $W$  shortens the timescale of changes in the local fluid motion experienced by the particle as it settles more rapidly through the turbulent eddies, and so enhances the effects of the particle inertia. Also shown in figure 8 in the same data with  $\langle \Delta V_1 \rangle$  scaled by  $u'$  and again the relative role of the large-scale fluid motion on the quantitative value is evident. Noticeably, the results under this scaling agree very well for the two flows on  $48^3$  and

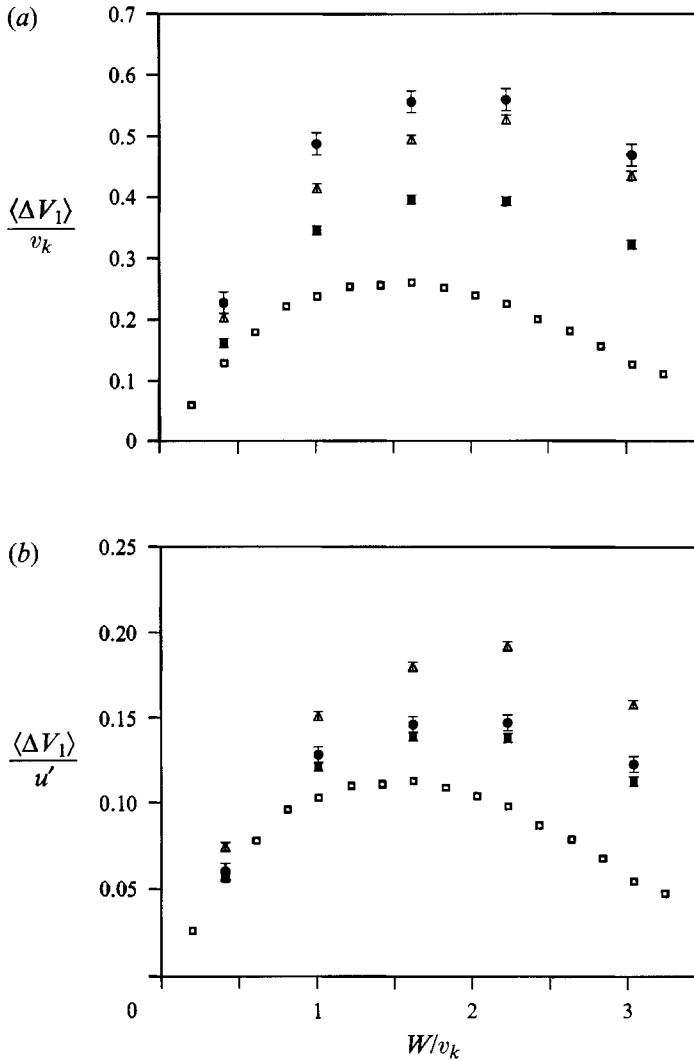


FIGURE 8. The increase  $\langle \Delta V_1 \rangle$  in the mean settling velocity as a function of  $W/v_k$  for a fixed ratio of  $\tau_a/\tau_k = 1$ . (a) Normalized by Kolmogorov velocity scale  $v_k$ ; (b) normalized by r.m.s. fluid velocity  $u'$ .  $\square$ ,  $32^3$ ,  $Re_\lambda = 21$ ;  $\blacksquare$ ,  $48^3$ ,  $Re_\lambda = 31$ ;  $\bullet$ ,  $96^3$ ,  $Re_\lambda = 62$ ;  $\triangle$ ,  $48^3$  and use of the second forcing scheme,  $Re_\lambda = 30$ . For the  $32^3$  simulations, the size of the symbol is made the same as the error bar.

$96^3$ , while those for  $32^3$  are much smaller. Figures 7 and 8 show that the different forcing schemes give different quantitative values although the qualitative features are the same. The larger quantitative increase in the settling velocity for the second forcing scheme may be partly due to the steady nature of the applied forcing and the smaller forcing radius used.

The above results are concerned only with the mean statistics of particle motion. In figure 9 the particle r.m.s. velocity  $\langle \sigma \rangle$  normalized by  $u'$  is shown as a function of  $\tau_a/\tau_k$ , for a fixed value of the terminal velocity  $W/v_k = 1.0$ . Here  $\sigma \equiv \frac{1}{3}(\langle \sigma_1 \rangle + 2\langle \sigma_2 \rangle)$  is an average over the three directions. In the simulations we found that  $\langle \sigma_1 \rangle$  is usually slightly larger than  $\langle \sigma_2 \rangle$  (see figure 4 for example) and is a consequence of the continuity effect (Reeks 1977). Since the difference between  $\langle \sigma_1 \rangle$  and  $\langle \sigma_2 \rangle$  is small for

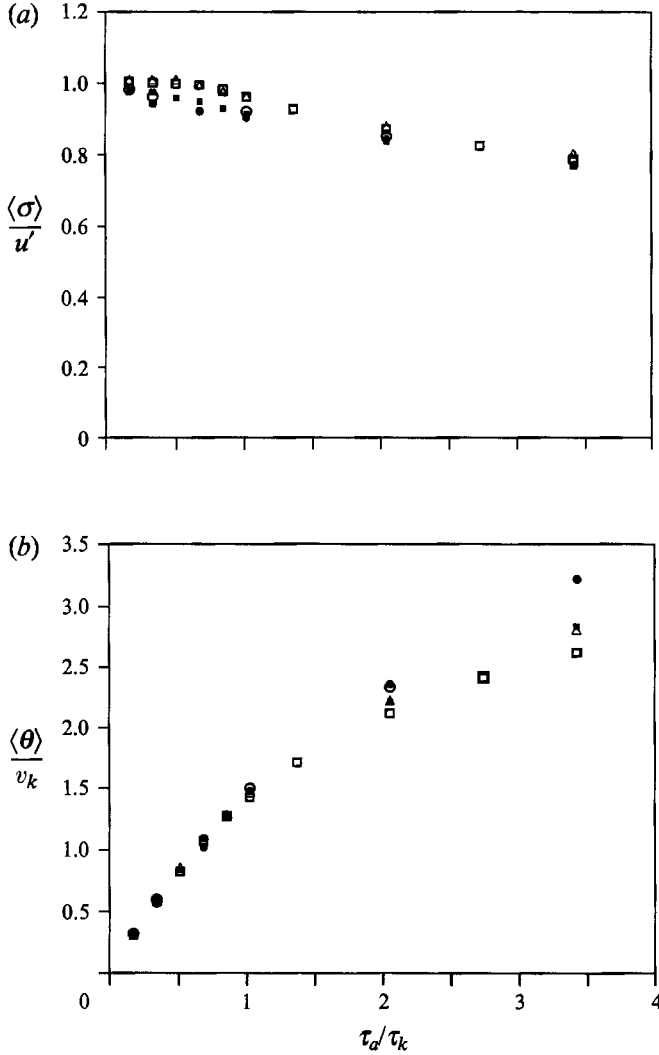


FIGURE 9. (a) The particle r.m.s. fluctuating velocity  $\langle \sigma \rangle$  normalized by  $u'$  as a function of  $\tau_a / \tau_k$ ; (b) the particle r.m.s. relative velocity  $\langle \theta \rangle$  normalized by  $v_k$  as a function of  $\tau_a / \tau_k$ .  $W/v_k$  is set to one for these simulations.  $\square$ ,  $32^3$ ,  $Re_\lambda = 21$ ;  $\blacksquare$ ,  $48^3$ ,  $Re_\lambda = 31$ ;  $\circ$ ,  $64^3$ ,  $Re_\lambda = 43$ ;  $\bullet$ ,  $96^3$ ,  $Re_\lambda = 62$ ;  $\triangle$ ,  $48^3$  and use of the second forcing scheme,  $Re_\lambda = 30$ .

the parameter range shown in figure 9, only the average value is discussed here. The r.m.s. particle velocity fluctuation decreases monotonically with increasing  $\tau_a / \tau_k$ , as the response of the particles to high-frequency (small scales) fluid motion diminishes. The quantitative value of the r.m.s. particle velocity fluctuation follows a scaling based on the large-eddy motion. Figure 9 further shows the r.m.s. relative velocity averaged over the three directions as a function of  $\tau_a / \tau_k$  for  $W/v_k = 1.0$ . Again the difference between the different directions is small and not the main concern here. Unlike the r.m.s. particle velocity, the relative velocity increases quickly with the particle response time and its quantitative value follows Kolmogorov scaling for  $\tau_a / \tau_k$  up to order one. Within this range the relative velocity is strongly influenced by small-scale fluid motions. For larger particle response time, the large-scale fluid motion also plays a

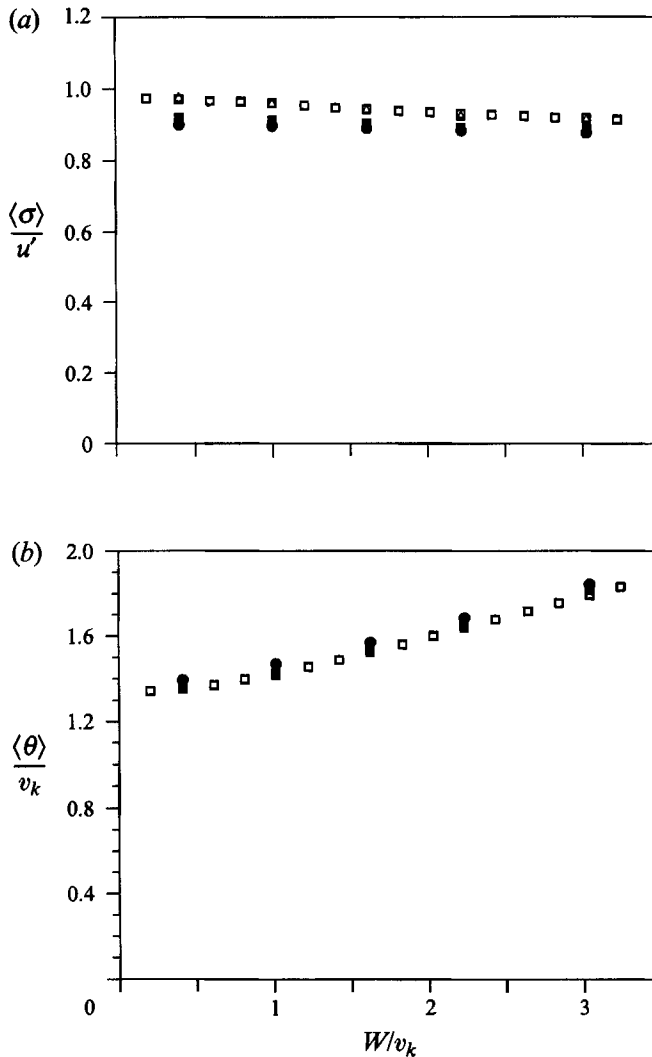


FIGURE 10. (a) The particle r.m.s. velocity  $\langle \sigma \rangle$  normalized by  $u'$  as a function of  $W/v_k$ ; (b) the particle r.m.s. relative velocity  $\langle \theta \rangle$  normalized by  $v_k$  as a function of  $W/v_k$ .  $\tau_a/\tau_k$  is set to one for these simulations.  $\square$ ,  $32^\circ$ ,  $Re_\lambda = 21$ ;  $\blacksquare$ ,  $48^\circ$ ,  $Re_\lambda = 31$ ;  $\bullet$ ,  $96^\circ$ ,  $Re_\lambda = 62$ ;  $\triangle$ ,  $48^\circ$  and use of the second forcing scheme,  $Re_\lambda = 30$ .

role. This is apparent from the larger values of  $\langle \theta \rangle/v_k$  as the Reynolds number is increased for any given value of  $\tau_a/\tau_k \geq 2$ . This corresponds to the broader range of scales and the presence of more larger-scale fluid motion at higher Reynolds number.

Figure 10 shows the corresponding data for the r.m.s. particle velocity and the relative velocity as a function of  $W/v_k$  for  $\tau_a/\tau_k = 1.0$ . The r.m.s. particle velocity decreases slowly with  $W/v_k$  as a result of increasing effective inertia. The relative velocity increases with  $W/v_k$  and agrees very well, under the Kolmogorov scaling, for different flow  $Re$  numbers.

In summary, we observe an increase in the mean settling speed of heavy particles in a uniform turbulence of zero mean velocity. The qualitative feature of the relative increase follows Kolmogorov scaling in terms of the values of the parameters  $\tau_a/\tau_k$  and

$W/v_k$  while the actual magnitude of the increase value may be affected by fluid motion of various scales.

#### 4.2. Concentration field and preferential sweeping

We shall now explore the mechanism for the faster settling rate observed. Since the particle motion is stationary after the initial transient interval, the mean particle velocity is time-independent and the equation of motion (3.1) gives

$$\langle \Delta V_1 \rangle = \left\langle \mathbf{u}(\mathbf{Y}(t), t) \cdot \frac{\mathbf{g}}{|\mathbf{g}|} \right\rangle. \quad (4.1)$$

The average  $\langle \mathbf{u}(\mathbf{Y}(t), t) \rangle$  is the ensemble averaged fluid velocity as measured following a particle trajectory. This average differs in nature from both a Eulerian, fixed-point average and a Lagrangian average following a fluid element. If the particle concentration field is uniform, this average fluid velocity reduces to the Eulerian spatial average of the fluid velocity, which should be zero for our simulated flows. The fact that this average was shown to be positive has two implications: (i) the long-time particle concentration field is not uniform and (ii) a particle may be found relatively more often in regions where the component of the flow velocity in the direction of gravity is positive. Indeed, both features were observed for heavy particles in a cellular flow (Maxey & Corrsin 1986). The inertial bias discussed by Maxey (1987) leads to such a non-uniform concentration and this was confirmed by the direct numerical simulations of Squires & Eaton (1991*b*) for the concentration field of heavy particles without gravitational settling. However, the first implication alone does not answer the question of the observed particle settling rate. In this subsection the particle concentration field for a typical case where both  $\tau_a$  and  $W$  are non-zero is investigated. Such a case has not been examined previously and it will allow us to verify the second implication in relation to the change in the settling rate.

Figure 11 shows the normalized particle concentration field and the scalar-vorticity field ( $\Omega \equiv (\omega_i \omega_i)^{1/2} / \langle (\omega_i \omega_i)^{1/2} \rangle$ ) at the five consecutive time frames (from top to bottom) on a plane section,  $x_3 = \pi$ ,  $0 \leq x_1, x_2 < 2\pi$ , starting from  $t = 0.18$ . As noted earlier, the concentration field is statistically stationary. The direction of gravity is in the positive  $x_1$ -direction. The concentration field is very non-uniform, regions of either near zero or at least twice the mean are both shown visually and account for a significant portion of the whole section. These fields may be compared with those shown previously in figure 5 for the initial period following the particles as an initially uniform distribution. A maximum concentration of about 20 ~ 50 times the mean are observed in the simulations. A comparison between the concentration of the  $\Omega$  field demonstrates that the regions of high vorticity correlate well with the regions of low particle concentration.

There is a further important feature in figure 11. The regions of higher particle concentration tend to appear as long, connected patches or sheets that are aligned vertically. At the second time frame, a long particle patch is clearly seen near the right vertical edge of the section. It then seems to be broken by the stretching and rotation of the vortical region near the patch. However, another patch forms by the fifth time frame in the left half of the box, where the local vorticity field has changed little during the time interval covered. The next question is how are these long patches formed and what is their relationship to the local flow field. Figure 12 shows vector plots of the velocities of those particles in the region of high particle concentration at the second time frame of figure 11. The starting point of each vector represents the position of a particle and the vector length denotes the magnitude of the particle velocity. The



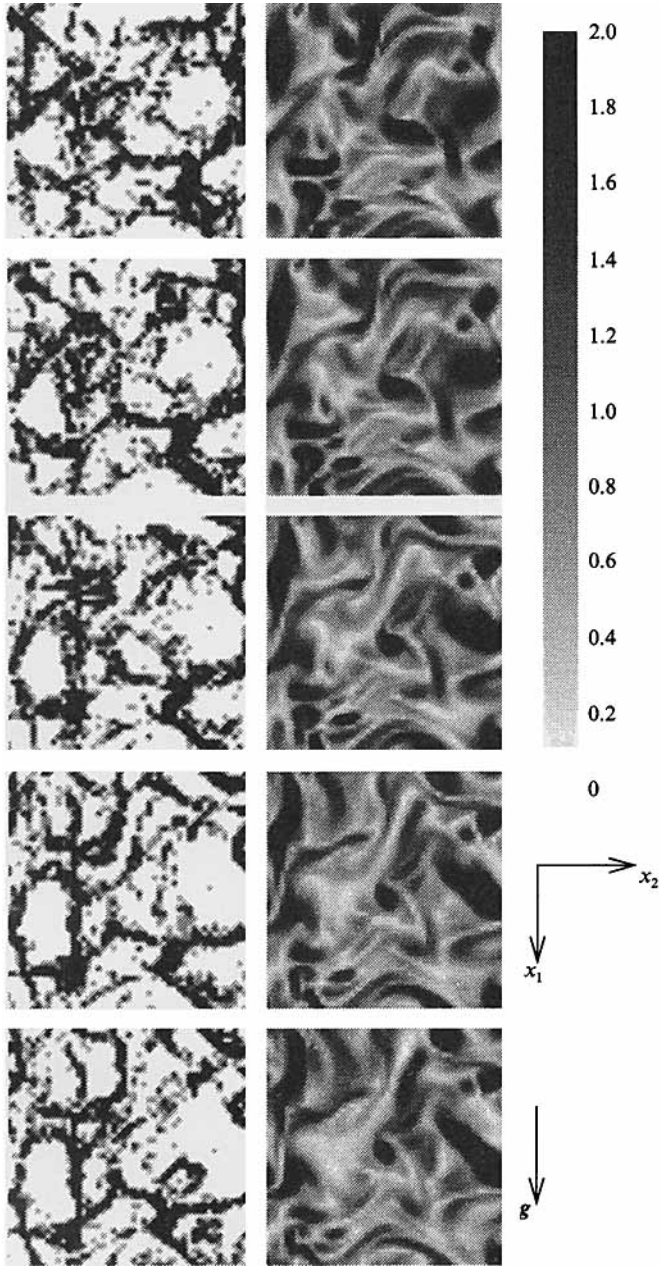


FIGURE 11. Normalized concentration field (left-hand side) and flow scalar-vorticity field (right-hand side) at five consecutive time frames (from top to bottom) in the  $(x_1, x_2)$ -plane at  $x_3 = \frac{1}{2}L$ , starting from  $t = 0.18$ . The time interval is 0.009, which is roughly equal to  $\tau_k$ . Note the time interval here is exactly half that in figure 5. The particle concentration field is expected to be stationary. Particle parameters are  $\tau_a/\tau_k = 1.0$  and  $W/v_k = 1.0$  and the grid resolution is  $48^3$ ,  $Re_\lambda = 31$ .

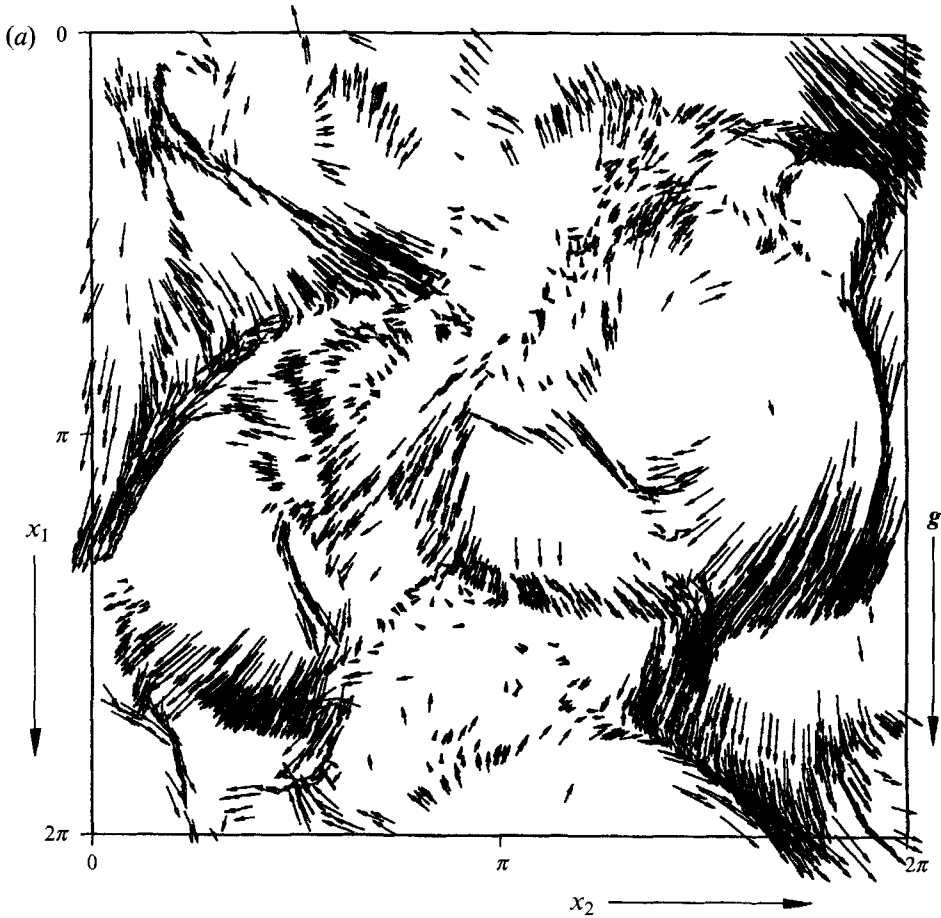


FIGURE 12 (a). For caption see facing page.

second plot of figure 12 gives the vector components of flow velocity field on the same plane together with some selected particle velocity vectors. The higher concentration 'sheet' formed by the clustered particles is located precisely in the channel-like, downflow regions in the velocity field which form between neighbouring regions of vorticity. This is a direct reason for the increase in the particle mean settling rate, consistent with the proposed second implication.

The reason for this preferential sweeping is illustrated by figure 13. Consider a heavy particle settling through a flow region with three local vortical structures as shown. The inertial bias implies that when encountering a vortical structure, the particle does not move along a flow streamline and has to make its path along the periphery of the vortical structure. With this in mind, now suppose the particle approaches the first vortical region at point *A*, the local induced flow velocity will move the particle to the right and thus the particle passes the first vortical region on the right, the downflow side. The process repeats as the particle approaches the second vortical region at point *B*. The particle may move to the right- or to the left-hand side of the region according to the local direction of fluid rotation. In either case, the particle tends to travel on the downflow side. Should a particle start to be swept upward by the local flow, for example, near the bottom of a vortical structure, it would begin to be entrained within the vortex and follow a closed path. This is countered by the inertial bias which causes

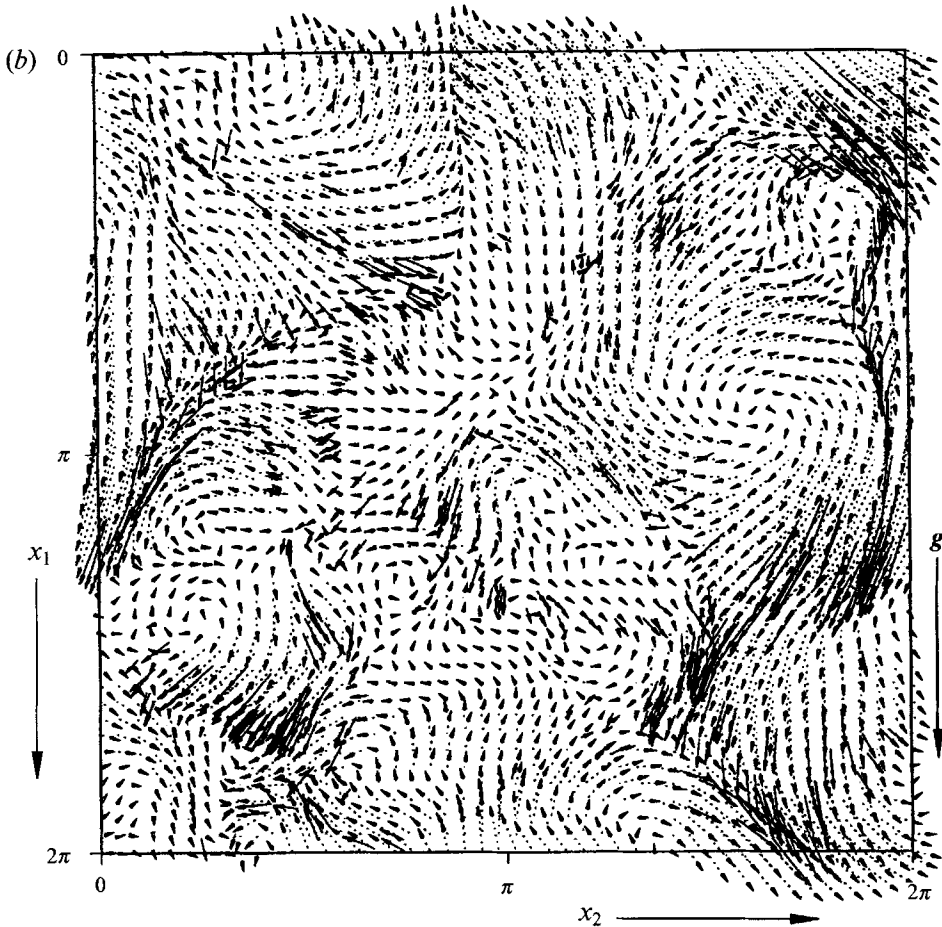


FIGURE 12. (a) The position and velocity plots at the second time frame shown in figure 11.3167 particles are found near the slice, i.e. in the region  $\pi - 0.5\delta < x_3 < \pi + 0.5\delta$ ,  $\delta$  is the grid spacing. The starting point of each vector arrow is the particle's position and the length of an arrow represents the relative magnitude of the velocity. (b) The vector velocity field (dot-line arrow) of the flow in the same plane overlaid by particle velocity vector (solid-line arrow) for those (621) particles within a distance of 10% grid spacing.

the particle to curve outwards away from the vortex. This response is surprisingly similar to the particle motion in cellular flows (Maxey & Corrsin 1986) even though these are steady and laminar. Without particle inertia there is no net effect on the average settling rate in a statistically homogeneous flow. In short, the preferential sweeping is due to the inertial bias, the local induced velocity field, and the fact that the particles approach them usually from above. In a turbulent flow the configuration of the flow structures changes with time and thus the formation of long particle patches depends on the relative persistence of the instantaneous structures. Ruetsch & Maxey (1992) examined the ability of the intense localized flow structures to mix a passive scalar. They found the persistence rather than the intensity of certain physical flow quantities, in this case the local straining rate, has a dominant effect on the generation of intense scalar gradient. Similarly, one may argue that persistent but not necessarily intense vortical structures can have a significant effect on the local particle transport. According to Hunt *et al.* (1987), a large part of a turbulent flow field may be classified

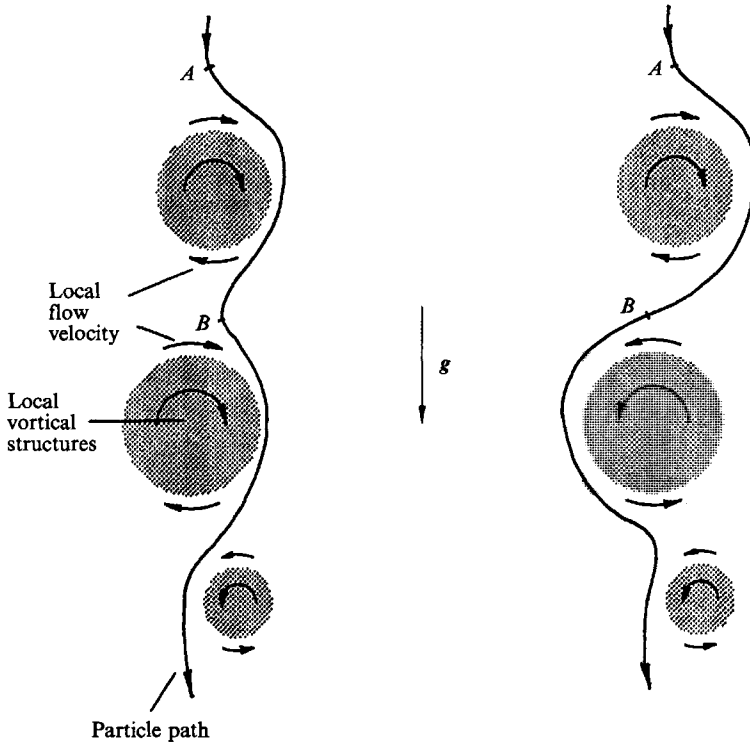


FIGURE 13. Sketch showing the preferential sweeping mechanism for a heavy particle interacting with local flow vortical structures under its inertia and body force.

into eddy, rotational, convergence or streaming zones. The above qualitative reasoning for preferential sweeping is relevant to the edges of eddy and rotational zones. Particles may be temporarily moved upwards by other flow zones, as can be seen in figure 11. Furthermore, the combined effect of inertia bias and preferential sweeping may send particles into streaming zones with downward fluid velocity. Since the largest scales contain most of the flow energy, the magnitude and configuration of the fluid velocity in the channel-like region of figure 12 is likely to be strongly affected by the large scales. A test was made to see to what extent the lower wavenumber range governed the fluid velocity field. This was done by low-pass filtering the velocity field of figure 12 in Fourier space, retaining only modes within the range  $0 < |\mathbf{k}| < 6$  and  $0 < |\mathbf{k}| < 3$  for this simulation on a  $48^3$ -grid. It was found that many of the general features were retained including the downflow streaming channel, and indicates the influence at this lower Reynolds number of the large-scale motions on the increase in the settling velocity.

We now proceed to quantify some aspects of the above observations. Figure 14 shows the correlation between the conditionally averaged concentration and the vorticity or the strain rate of the flow. The plot was constructed in the following way. The normalized scalar-vorticity  $\Omega$  value was divided into one of many bins,  $0.1(m-1) \leq \Omega < 0.1m$ ,  $m = 1, 2, 3, \dots$ ; then all the  $48^3$  grid points at each time frame were scanned to find the number of grid points,  $n(m)$ , where the value  $\Omega$  fell into the range for the  $m$ th slot. The conditionally averaged concentration for this slot was then defined as the number of particles counted on these  $n(m)$  grid points divided by  $n(m)$ . The process was repeated for 10 time frames starting from  $t = 0.180$  with an interval

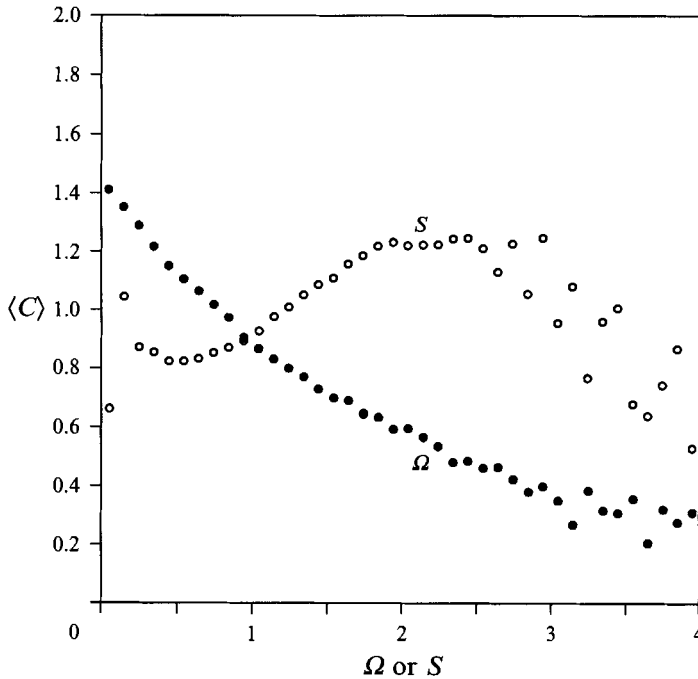


FIGURE 14. Correlation between the local particle concentration and the flow vorticity  $\Omega$  or the rate of strain  $S$  as given by the conditionally averaged concentration  $\langle C \rangle$ .

of 0.009, the data shown in figure 14 is actually an average over these ten frames. The same was done for the normalized rate of strain, with  $S = (s_{ij} \cdot s_{ij})^{1/2} / \langle (s_{ij} \cdot s_{ij})^{1/2} \rangle$ , where  $s_{ij} = \frac{1}{2}(\partial u_i / \partial x_j + \partial u_j / \partial x_i)$ . The results demonstrate that regions of higher concentration are well correlated (monotonically) with the regions of lower vorticity. It is also shown that the region of higher concentration is correlated with the region of higher rate of strain for  $0.5 < S < 2.5$ . For larger values of  $S$  the correlation between the concentration and the rate of strain seems to diminish. This may be related to the observation that regions of high strain-rate often surround the vortex tubes that characterize the regions of more intense vorticity (Ruetsch & Maxey 1991).

Similarly, we present in figure 15 the correlation between the concentration and the fluid velocity near the particles. While there is no noticeable bias between the positive and the negative values in the horizontal fluid velocity  $u_2$ , a clear bias is seen in the vertical fluid velocity  $u_1$ . The vertical fluid velocity for the higher concentration regions tends to have a positive value. Since the gravity is oriented in the  $+x_1$  direction, this is just a restatement that particles are found more often in the downflow regions than in the upflow regions.

The above discussion indicates that preferential sweeping in addition to preferential concentration due to inertial bias results in the faster settling rate. What is surprising is the similarity of these processes in an evolving turbulent flow and the results for the steady cellular flow fields of Maxey & Corrsin (1986).

#### 4.3. Kolmogorov scaling of local accumulation

We now quantify the degree of local accumulation directly to find out under what condition the strongest local accumulation occurs. Qualitatively the local accumulation is related to the notion of inertial bias, i.e. the interaction of particles with flow vorticity

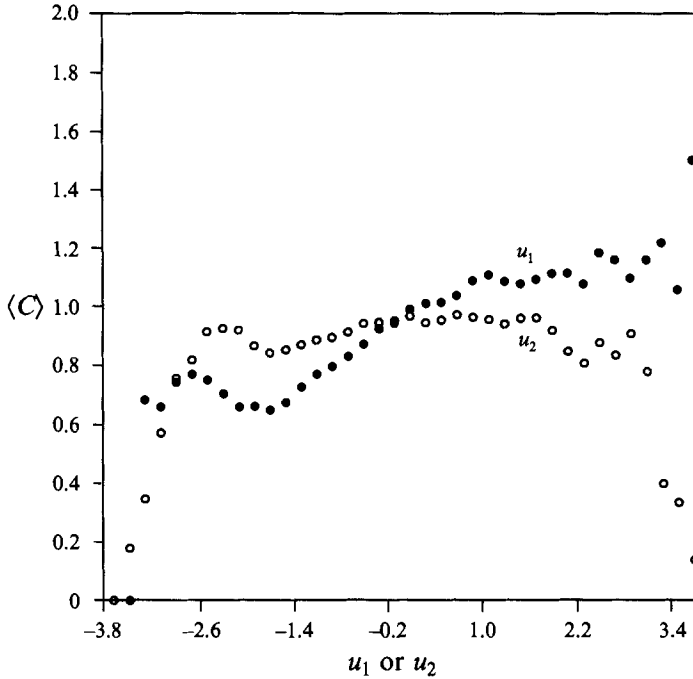


FIGURE 15. Correlation between the local particle concentration and the vertical or horizontal fluid velocity as given by the conditionally averaged concentration  $\langle C \rangle$ . Note the gravity is assigned in  $+x_1$  direction.

field, in particular the intense vortical regions. As the intense vortical regions are a feature of the small-scale, dissipation-range flow dynamics (She *et al.* 1990), the degree of this inertial bias is likely to be maximized when the particle parameters are comparable to the dissipation-range scales, namely the Kolmogorov scales. In the study of Squires & Eaton (1991*b*), the particle response time was normalized by the integral timescale of the flow,  $T_f \equiv L_f/u'$ . They studied the particle concentration field at three particle parameters  $\tau_a/T_f = 0.075, 0.150, 0.520$  (all for zero  $W$ ) and found that the degree of non-uniformity of the concentration field owing to inertia bias was the greatest at  $\tau_a/T_f = 0.150$ . If we re-normalize the particle response time by the Kolmogorov scale in their simulation, the three cases are  $\tau_a/\tau_k = 0.326, 0.651, 2.26$ . Then their results suggest that the degree of local accumulation is the greatest when  $\tau_a/\tau_k$  is close to one. Thus their results are consistent with the hypothesis for Kolmogorov scaling for the local accumulation. In this section global measures of local accumulation are developed to verify the above hypothesis.

We start with the two probability functions introduced in §2.3. Figure 16 shows the two probability functions computed from a typical simulation at  $t = 0.216$  for the case of  $\tau_a/\tau_k = W/v_k = 1$ . The exact solution for the case of uniform concentration is shown as a comparison. The probability of finding a void region with no particles,  $P_c(C = 0)$ , is 0.5824, almost twice the value for the random uniform distribution case, see (3.15).  $P_c$  is smaller than the value of  $P_c^u$  for intermediate concentrations,  $C = 1, 2, 3$ , but larger for  $C \geq 4$ . The relative contribution of a given concentration to the total number of particles,  $P_n$ , is also very different from  $P_n^u$ . It was computed that  $P_c(C \leq 2) = 84\%$  yet  $P_n(C \leq 2) = 29\%$ . This means that most of the particles are located in

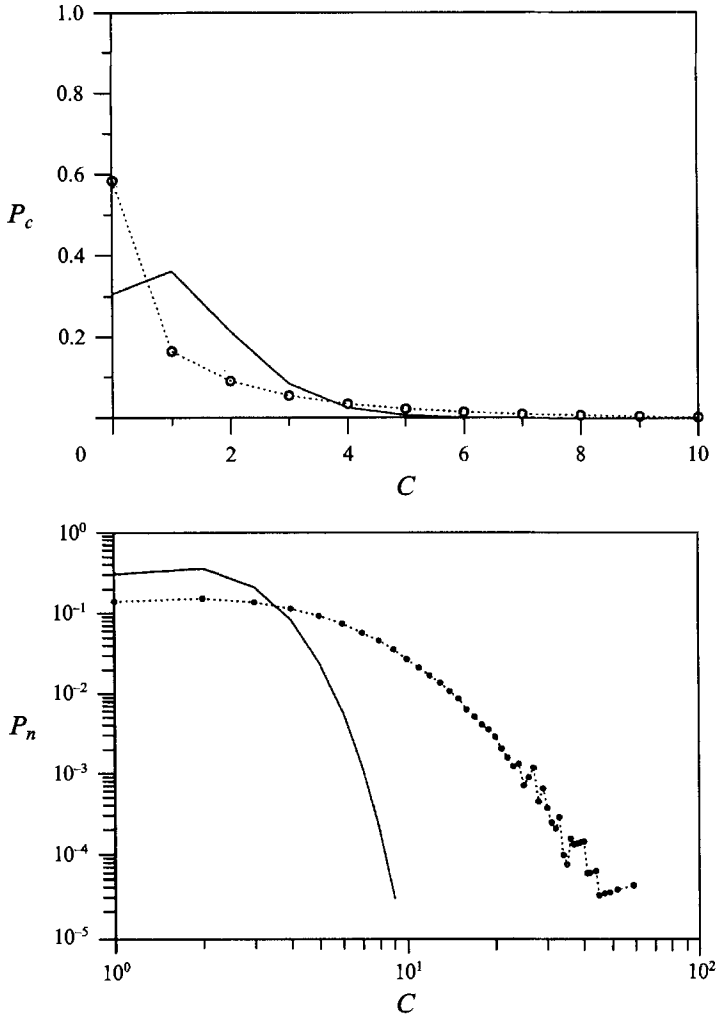


FIGURE 16. Probability functions  $P_c$  and  $P_n$  against  $C$ , computed at time  $t = 0.216$ , for  $\tau_a/\tau_k = 1 = W/v_k$  on  $48^3$  grid for  $Re_\lambda = 31$ ; the results for a uniform random distribution shown as a solid curve.

a small portion of space where the concentration is much greater than the mean. The maximum concentration observed here is 59, about 50 times the mean concentration.

Clearly the differences between the probability functions and their respective values for the random distribution case are what really measure the local accumulation. Therefore, we introduce a global measure of local accumulation as an integrated square deviation for each probability function,

$$D_c = \sum_{C=0}^{N_p} (P_c(C) - P_c^u(C))^2, \quad (4.2)$$

$$D_n = \sum_{C=0}^{N_p} (P_n(C) - P_n^u(C))^2. \quad (4.3)$$

Each of these provides a single number that quantifies the local accumulation. Furthermore, these global measures are expected to be computed accurately even when

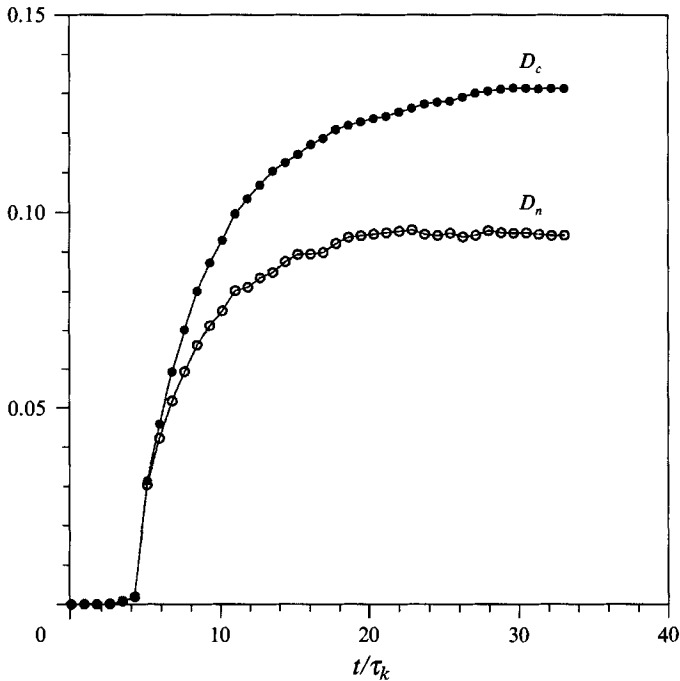


FIGURE 17. The two global measures  $D_c$  and  $D_n$  of local particle accumulation as a function of  $t/\tau_k$  for  $\tau_a/\tau_k = W/v_k = 1$ .

the total number of particles is not large as compared to that needed for a reasonable visual representation of the concentration field. In this sense, they are more useful than the probability functions.

Figure 17 shows how the global measures change with time for the case of  $\tau_a/\tau_k = W/v_k = 1$ . They increase with time monotonically. For  $t/\tau_k < 4$  they show little change, indicating that a certain time is needed for the particles to adjust their initial velocity to the local flow field. A rapid change occurs for the interval  $3.8 < t/\tau_k < 9.5$  when the particles respond efficiently to the dynamics of flow structures, which agrees with the qualitative features observed in figure 5. The measures then change slowly and level off to asymptotic values. Intuitively, the asymptotic values represent a balance between the accumulation due to local vortical structures and random stirring at large scales. We note that  $D_n$  is relatively flat while  $D_c$  still increases slowly for  $t/\tau_k > 20$ . In §3.2, the average settling rate is found to reach its asymptotic value for  $t > 2T_e$ . Here we observe that small final adjustment in the concentration distribution is likely even for  $t > 2T_e$ . The behaviour of the mean settling rate with time is arguably related more directly to  $D_n$  rather than  $D_c$ , thus these results are consistent.

We are now in a position to show the dependence of  $D_c$  and  $D_n$  on particle parameters. In figure 18,  $D_c$  and  $D_n$  are plotted as a function of particle response time for a fixed  $W/v_k$  at various times. The particles have the same initial distributions. Of significance is the fact that both  $D_c$  and  $D_n$  reach a maximum around  $\tau_a/\tau_k \approx 1.0$ , a feature that becomes very clear in the long term when the concentration field is approximately statistically stationary. This further supports the hypothesis of Kolmogorov scaling for the local accumulation. The time for the asymptotic value of the measures to become established seems to be independent of the particle inertial response time over the parameter range studied. We note the timescale separation in



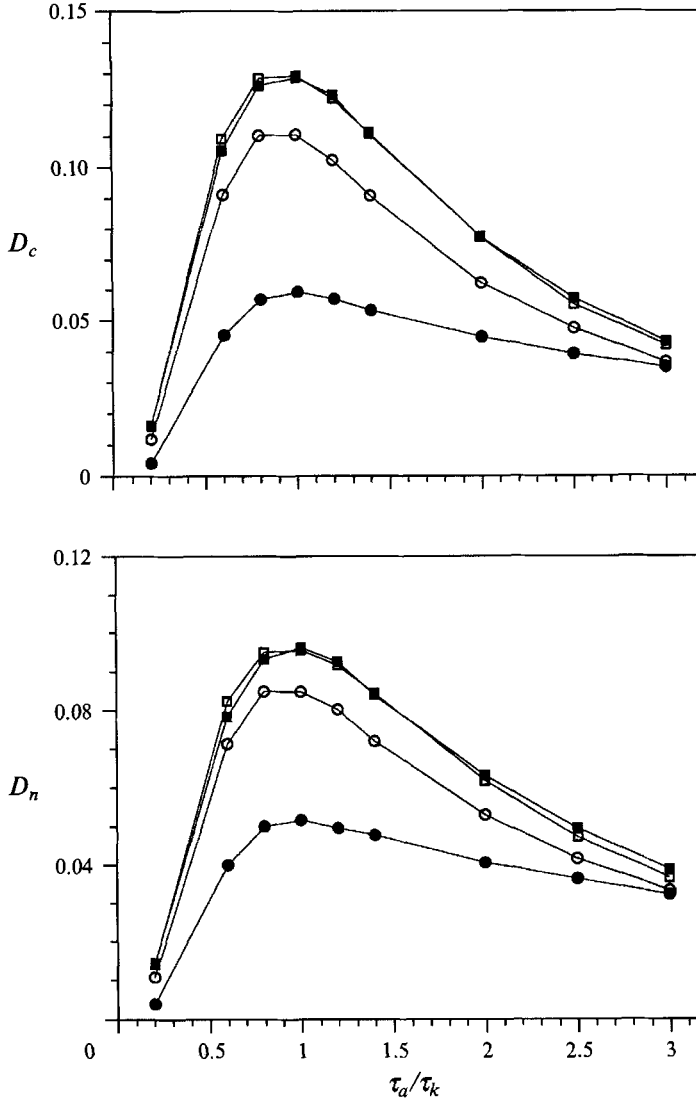


FIGURE 18. The two global measures of local particle accumulation as a function of particle inertial timescale  $\tau_a/\tau_k$  for a fixed ratio of  $W/v_k = 1$ .  $\bullet$ ,  $t/\tau_k = 6.8$ ;  $\circ$ ,  $t/\tau_k = 13.6$ ;  $\blacksquare$ ,  $t/\tau_k = 20.4$ ;  $\square$ ,  $t/\tau_k = 27.2$ . Simulations are performed on  $48^3$  grid,  $Re_\lambda = 31$ .

the flow field,  $T_e/\tau_k$ , is about 8; at this value of  $\tau_a/\tau_k$  the degree of local accumulation would be expected to be very small compared to the maximum. In this regard, the flow scale separation is adequate for us to draw the conclusion of Kolmogorov scaling. This Kolmogorov scaling partly explains why the relative increase in the settling rate is maximized when the particle parameters are comparable to flow Kolmogorov scales. The degree of local accumulation only slightly depends on the terminal velocity, as shown in figure 19. This is different from the dependence of  $\langle \Delta V \rangle$  on the terminal velocity of figure 8. The value of  $\langle \Delta V \rangle$  should be small for small  $W$ , as in this case the particle fluctuation velocity may be much larger than  $W$  and the preferred direction for the particle to approach a local structure is lost, i.e. the preferential sweeping effect is weak. While for large  $W$ , the relative residence time for a particle to interact with a

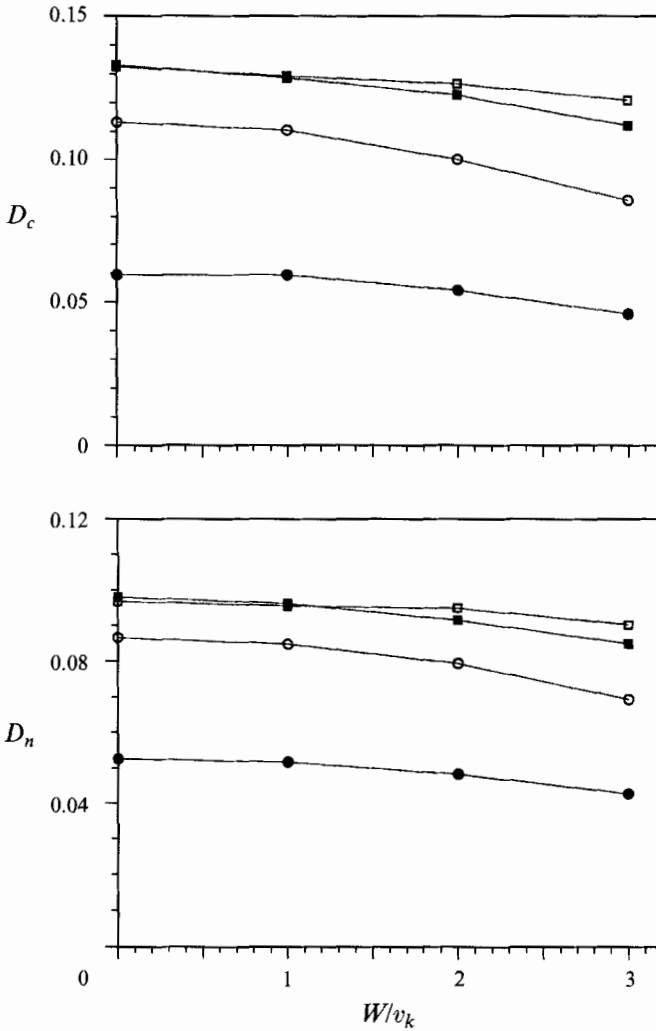


FIGURE 19. The two global measures  $D_c$  and  $D_n$  of local particle accumulation as a function of the terminal velocity for a fixed ratio of  $\tau_a/\tau_k = 1$ .  $\bullet$ ,  $t/\tau_k = 6.8$ ;  $\circ$ ,  $t/\tau_k = 13.6$ ;  $\blacksquare$ ,  $t/\tau_k = 20.4$ ;  $\square$ ,  $t/\tau_k = 27.2$ . Simulations are performed on  $48^3$  grid,  $Re_\lambda = 31$ .

local structure is short and again  $\langle \Delta V \rangle$  should not be large. This would be a reason for the much stronger dependence of  $\langle \Delta V \rangle$  than  $D_c$  (or  $D_n$ ) on  $W$ . Consequently, the inertial bias or local accumulation is only a part of the reason for the observed faster settling.

The above discussions are restricted to the  $48^3$  grid. We may compute in a similar manner the global measures on the  $96^3$  grid at a higher Reynolds number based on the amount of particles used for the settling rate computation (§3.2), i.e. compute  $D_c$  and  $D_n$  with 4096 particles and then average over the six orientations. Figure 20 shows the results. Note the values of  $D_c$  and  $D_n$  are very small because of the number of particles and the grid resolution, but the relative uncertainty is expected to be comparable to that associated with the settling rate of figure 7. Thus the results are still meaningful although the concentration field cannot be adequately simulated with this number of particles. The overall features in figure 20 are similar to that of figure 18. At this

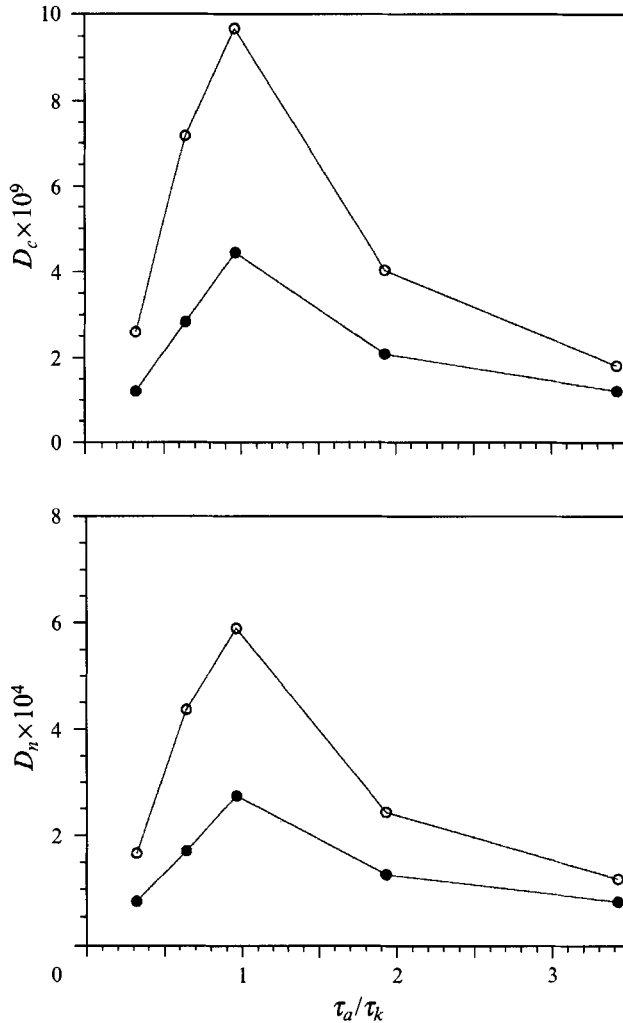


FIGURE 20. The two global measures  $D_c$  and  $D_n$  of local particle accumulation as a function of particle inertial time for  $96^3$  grid,  $Re_\lambda = 62$ ,  $W/v_k = 1$ . Only  $6 \times 4096$  particles are followed, as in the computation of mean settling rate.  $\bullet$ ,  $t/\tau_k = 20$ ;  $\circ$ ,  $t/\tau_k = 60$ .

Reynolds number the separation of flow timescales is much greater, the ratio of  $T_e/\tau_k$  is now about 16. But in both figures 18 and 20 the peak accumulations occur around  $\tau_a/\tau_k = 1$ .

In summary, the changes in settling velocity and the local accumulation of particles are more features of small-scale turbulence processes than large scales. This is in contrast to the problem of particle dispersion which is dominated by the bulk stirring of the large scale eddies.

## 5. Effect of nonlinear drag

In the preceding discussions the fluid drag force on the particle has been based on a linear, Stokes drag law. More generally, a nonlinear relation for the drag force, dependent on the particle Reynolds number, should be used if this Reynolds numbers is not small. In this section a brief discussion is given of the modifying effects of such

a nonlinear drag force relation on the average particle settling velocity. A problem that immediately arises is exactly what is the appropriate representation of the fluid force on the particle as it accelerates in a non-uniform flow field when the particle Reynolds number is not small. This is a limitation of the theoretical analysis of retarded settling for particles in simple oscillatory flows mentioned earlier in §1 (Tunstall & Houghton 1968; Schöneborn 1975; Hwang 1985). A commonly used representation is that of Odar & Hamilton (1964) but this has not been entirely satisfactory. Recent computational studies by Rivero (1991) and Chang (1992) on the unsteady flow past a sphere may help to resolve these issues.

For the present we shall adopt an empirical relationship for  $f(Re_p)$  based on the instantaneous value of the particle Reynolds number  $Re_p$ ,

$$f(Re_p) = 1 + 0.15Re_p^{0.687}. \quad (5.1)$$

This relationship given by Clift *et al.* (1978) is valid for values of  $Re_p < 40$  under steady flow conditions to within about 5%. It follows that the terminal velocity,  $W^{(T)}$ , in still fluid satisfies

$$W^{(T)} \left[ 1 + 0.15 \times \left( \frac{d_p W^{(T)}}{\nu} \right)^{0.687} \right] = \tau_a g. \quad (5.2)$$

Thus  $W^{(T)}$  is, in general, different from the Stokes settling velocity  $W = \tau_a g$ . The particle Reynolds number may be written as

$$Re_p = \left( \frac{18\tau_a}{\nu\rho_p/\rho_f} \right)^{\frac{1}{2}} \times |V - \mathbf{u}|. \quad (5.3)$$

Noting that the viscosity  $\nu$  is related to the Kolmogorov scales by  $\nu = \tau_k v_k^2$ , we obtain

$$Re_p = 4.243 \left( \frac{\rho_p}{\rho_f} \right)^{-0.5} \times \left( \frac{\tau_a}{\tau_k} \right)^{0.5} \times \frac{|V - \mathbf{u}|}{v_k}. \quad (5.4)$$

Therefore, only the density ratio needs to be added in the parameterization of the effect of nonlinear drag. For the remaining calculations we take a typical value of  $\rho_p/\rho_f = 877$  for water droplets in air (a higher density ratio will result in an even weaker effect of drag nonlinearity for the parametric range studied here). All the simulations in this section were performed on the  $48^3$  grid at  $Re_\lambda = 31$ .

As we are mainly interested in the range where the particle inertial time  $\tau_a$  is of the order of  $\tau_k$  which is much less than the large-scale eddy turnover time, we anticipate that the particle responds reasonably well to the overall local fluid velocity fluctuations, which implies  $\langle |V - \mathbf{u}| \rangle \approx \langle V_1 \rangle \approx W^{(T)}$ . We can then estimate that the average value of  $Re_p$  varies from 0 to 1 for  $0.0 < \tau_a/\tau_k < 3$  and  $0 < W/v_k < 4$ . It is possible, however, that the maximum  $Re_p$  value can be (or much) larger than the above range. (The actual range will be given below.) Nevertheless, the effect of nonlinear drag is to modify only slightly the results of settling rate, as will be shown in the following. The CPU time for the extra computations of nonlinear drag coefficient was found to be negligible compared to the total time.

Figure 21 compares the simulation results utilizing the nonlinear drag with corresponding results for the linear drag. Several interesting observations can be made. In §4.1, we only present results for a single fixed value of  $\tau_a/\tau_k$  as  $W/v_k$  is varied. Figure 21 shows that for other fixed  $\tau_a/\tau_k$  values and the use of the linear drag,  $\langle \Delta V_1 \rangle$  depends on  $W/v_k$  in a similar manner to the case of  $\tau_a/\tau_k = 1$ . In particular, the maximum  $\langle \Delta V_1 \rangle$  is attained at about the same  $W/v_k$ .  $\langle \Delta V_1 \rangle$  approaches zero rather slowly for large

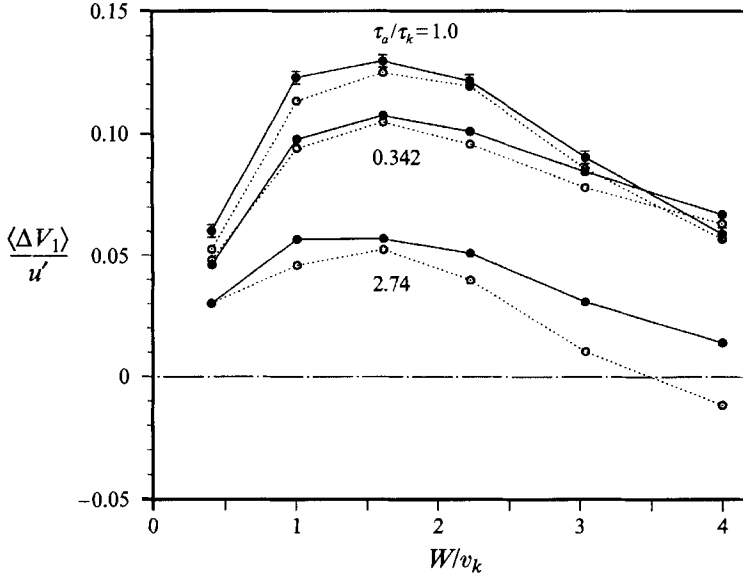


FIGURE 21. The relative increase in the mean settling velocity as a function of  $W/v_k$  for three different inertial response times  $\tau_a/\tau_k = 0.342, 1.0, 2.74$ : ●, linear drag force; ○, nonlinear drag force.

settling rate as the relative inertial response time becomes small. Secondly, the results for the nonlinear drag case ( $\Delta V_1 = V_1 - W^{(T)}$ ) is only slightly different from (less than) those based on the linear drag. The difference becomes larger for larger  $\tau_a$  and large  $W$ . While an increase in the settling rate is always observed for the linear drag case, a net decrease in the settling rate occurs for one case ( $\tau_a/\tau_k = 2.74$  and  $W/v_k = 4.0$ ) under nonlinear drag. This net reduction is explained in the following.

We can approximate the equation of motion as

$$\frac{dV}{dt} \approx \frac{\langle f \rangle [\mathbf{u}(\mathbf{Y}, t) - V] + \tau_a \mathbf{g}}{\tau_a}, \quad (5.5)$$

where the fluctuation in  $f$  is neglected, which is a valid approximation as shown later. The mean settling velocity is then

$$\langle V_1 \rangle \approx \langle \mathbf{u}(\mathbf{Y}, t) \rangle + \frac{\tau_a \mathbf{g}}{\langle f \rangle}. \quad (5.6)$$

The still fluid settling velocity may be written as

$$W^{(T)} = \frac{\tau_a \mathbf{g}}{f^s}, \quad (5.7a)$$

where

$$f^s = 1 + 0.15 \times \left( \frac{2aW^{(T)}}{\nu} \right)^{0.687}. \quad (5.7b)$$

The relative change in the settling rate under nonlinear drag may result from two reasons. The first is due to the preferential sweeping mechanism that is represented by a non-zero, positive  $\langle \mathbf{u}(\mathbf{Y}, t) \rangle$  as discussed for the linear drag case. This increases the particle settling rate. The second is related to the difference between  $\langle f \rangle$  and  $f^s$  resulting from the fluid turbulence fluctuations. The nonlinear factor  $\langle f \rangle$  must be slightly larger than  $f^s$  owing to the larger fluctuating slip velocities that arise when the

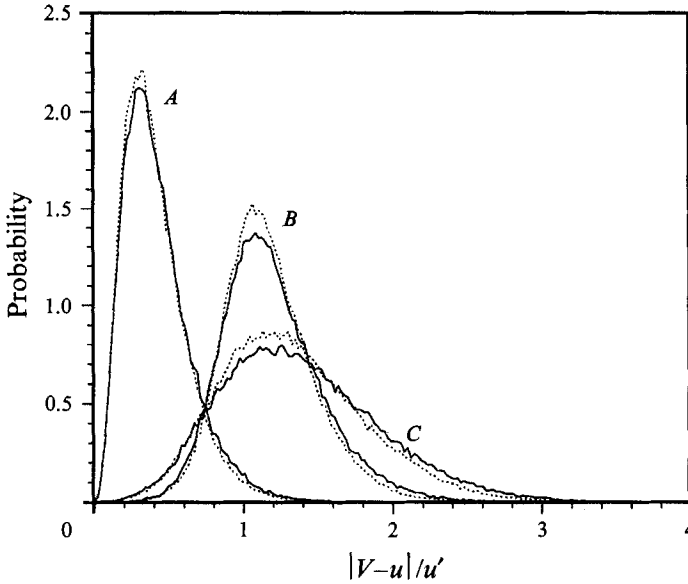


FIGURE 22. The probability distribution of the slip velocity of both —, the linear and  $\cdots$ , the nonlinear drag. *A*:  $\tau_a/\tau_k = 1.0$ ,  $W/v_k = 0.4$ ; *B*:  $\tau_a/\tau_k = 1.0$ ,  $W/v_k = 3.0$ ; *C*:  $\tau_a/\tau_k = 2.7$ ,  $W/v_k = 3.0$ .

particle is in a turbulent flow. This second effect, opposite to the preferential sweeping, reduces the settling rate and exists even when the first effect is not present. This relative reduction associated with the drag nonlinearity has been realized earlier by Tunstall & Houghton (1968) and Hwang (1985) in simple oscillatory flows and recently by Mei (1990) for random flow fields. This is the reason for a slightly smaller  $\langle \Delta V_1 \rangle$  when the nonlinear drag is used. Obviously, it is possible to observe a net settling rate reduction when the drag nonlinearity effect offsets the preferential sweeping effect. Finally, we note that the nonlinear drag can also modify the quantitative value of the bias term  $\langle \mathbf{u}(Y, t) \rangle$  since the effective particle inertia response time is slightly reduced ( $\tau_e = \tau_a / \langle f \rangle$ ). This coupling may either reduce or enhance the bias term depending on the particle response time relative to  $\tau_k$  (see figure 7).

To substantiate the above reasoning, we computed the p.d.f. distribution for the slip velocity  $|V-u|$  shown in figure 22. The distributions are computed based on 49152 independent data points and when the particle motion is stationary. For all three parameter sets, the distribution for the nonlinear drag is slightly more concentrated than the corresponding linear drag case. This is due to the fact that the effective inertial response time is smaller for the nonlinear drag case and as such the particle follows more closely the local fluid fluctuations. The distribution is broader as either the response time or the terminal velocity is increased. Further statistics, such as the mean slip velocity,  $\langle f \rangle$  and the r.m.s. fluctuating value of  $f$ , denoted by  $f'$ , can be easily computed using the distribution of the slip velocity and are displayed in table 2; also listed is the extreme case with a net settling rate reduction. First we notice that the maximum slip velocity realized in the simulations is quite large, resulting in the maximum  $Re_p$  being as large as about 3. The mean  $Re_p$  is at most  $O(1)$ . Both the mean slip and the maximum slip velocity for the nonlinear drag case are slightly less than those for the linear drag case owing to a lower effective inertial response time. The standard deviation of  $f'$  is at most 3% of  $\langle f \rangle$ . Most importantly,  $\langle f \rangle$  is larger than  $f^s$  by about 2%. When the inertial bias is small and  $W$  is large, such as for the case of

$(\tau_a/\tau_k, W/v_k)$	$\frac{\langle  V-u  \rangle}{u_0}$	$\frac{ V-u _{max}}{u_0}$	$Re_p$	$Re_{p,max}$	$\langle f \rangle$	$f^*$	$\frac{f'}{\langle f \rangle}$
(1.0, 0.4)	0.411 (0.426)†	1.986 (2.150)	0.170	0.823	1.0432	1.0216	0.015
(1.0, 3.0)	1.169 (1.191)	3.104 (3.371)	0.484	1.286	1.0905	1.0856	0.015
(2.7, 3.0)	1.325 (1.379)	4.069 (4.270)	0.909	2.790	1.1384	1.1211	0.031
(2.7, 4.0)	1.624	4.469	1.114	3.065	1.1598	1.1462	0.030

† The data in the parentheses are the corresponding value for the same  $\tau_a$  and  $W$  and when the linear Stokes drag is used.

TABLE 2. Statistics for simulations with the nonlinear drag

$\tau_a/\tau_k = 2.7$  and  $W/v_k = 3.0$ , the change in the settling rate due to this difference in the  $f$  is given as  $W(f^* - \langle f \rangle)/f^*$  (about  $0.02u_0$ ) and can be important. The quantitative difference in the settling rate change between the nonlinear drag and the linear one shown in figure 21 at  $\tau_a/\tau_k = 2.7$  and  $W^*/v_k = 3.0$  is consistent with this estimation.

In summary, the effect of nonlinear drag in the present study where  $Re_p$  is  $O(1)$  is to slightly reduce the settling rate increase compared to the case for linear drag. The bias term dominates the settling rate change and we still observe a net increase in the settling rate, except for one set of particle parameters.

## 6. Concluding remarks

The average settling rate of heavy particles suspended in a turbulent flow has been computed, using the velocity field obtained from direct numerical simulations. It is shown that the settling rate is greater than the terminal velocity in still fluid, which is consistent with the results in a random flow field (Maxey 1987). However, the relative increase in the settling rate is found to be as high as 40 ~ 50 % of the terminal velocity and much larger than that found in the previous study. A major distinction between the present study and that based on a random flow field is that here the flow evolves dynamically with the appropriate spatial and temporal structures, including the organized features of the dissipation range dynamics. In the random flow fields there was no such dynamical organisation, even though the averaged energy spectrum was prescribed. While for all our simulations,  $T_E$  is comparable to  $T_e$  or  $L_f/u'$  (see Yeung & Pope 1989); according to the results of Maxey (1987), the relative change in the settling rate should be very small. Our results, however, suggest that a much larger increase in the settling rate is possible even when  $T_E \sim L_f/u'$ . This implies that the dynamical interactions of particles with coherent eddy structures are much stronger than in the case of random flow field and possibly last over a longer period of time. The results presented here demonstrate that the maximum increase occurs when the particle parameters are made comparable to the flow Kolmogorov scales. The mechanism by which the settling rate changes is due to the two physical processes. First, the inertial bias causes particles to accumulate in the peripheries of local vortical structures, and this characterizes in large part the direct interactions of heavy particles with the small-scale, dissipation-range flow dynamics. Secondly, the particles tend to move on the downflow sides of such local structures due to a combination of the local velocity field, particle inertia, and the fact that the particles approach them usually from above. The

above processes may oversimplify the motion of heavy particles in turbulence, but they are nevertheless the essential features for the settling rate. We also quantify the degree of local accumulation due to inertial bias and reveal that it does follow Kolmogorov scaling, namely, the strongest accumulation happens when the particle response time is comparable to the Kolmogorov timescale.

This Kolmogorov scaling indicates that the small-scale flow dynamics plays a significant role on certain aspects of particle transport in fully developed turbulence. This is in contrast with the traditional approach that the large-scale, energy-containing fluid motions dominate the transport of particles, in particular, the dispersion process. This does not invalidate the traditional approach, but implies that the traditional approach may not be adequate for many aspects of multiphase flow processes. We have demonstrated here that at least when the settling rate and local accumulation are considered, a proper account of small-scale flow dynamics is essential. There are other problems, such as the degree of mixing of heavy particles, where the small-scale flow dynamics cannot be overlooked. Further, we hope the present study indicates that the structural view of turbulent flows can contribute to the development of multiphase flow modelling, in addition to the more commonly used statistical view.

Two quite different forcing schemes have been used to provide flow energy at large scales. The qualitative features of the results are the same while the quantitative values differ. Further, the qualitative features are not altered as the flow Reynolds number is changed. Although only turbulent flows at moderate Reynolds numbers, noticeably lacking any inertial subrange, can be studied in the present approach we anticipate the same qualitative features will be observed for higher-Reynolds-number turbulent flows. Quantitative features of local accumulation await future investigations and establishment owing to the limited Reynolds number range that has been used here. However, this may be of secondary importance. In naturally occurring turbulent flows such as atmospheric turbulence, the flow scales are widely separated so the settling rate of small aerosols or droplets is likely to be affected only by a limited range of flow scales near the dissipation range. A few cases in this study have implied this situation. A wider scale separation implies that the vortical structures are more localized spatially. Then the particle–vortical structure interactions become a truly local phenomenon. Just as the small-scale features of turbulence, the dissipation-range dynamics, and the inertial-range dynamics all bear some universal properties, the qualitative aspects of the results presented here can also be regarded as universal. In fact, for extremely high-Reynolds-number flows, even the quantitative values can be independent of the large-scale fluid motions and thus some universal scaling would apply.

There are a number of other inferences that may be drawn from the present study. The effect of intense and persistent local vortical structures can modify quickly the particle concentration field near these local regions. In a shear mixing layer the organized, large-scale vortical structures can greatly influence the global transport, dispersion, and mixing of heavy particles (Wang *et al.* 1992). The small-scale vortical structures in turbulent flows may have a similar effect on the local transport and mixing of heavy particles. The strong local accumulation of particles may also significantly enhance the local flow dissipation in two-phase systems, indicating that the local feedback effect of heavy particles on the turbulence may be significant for a gas–solid particle system even at a nominally low mass-loading. By the same consideration, the particle–particle interactions may also be important locally.

We are grateful to Dr G. R. Ruetsch for his help with the turbulence code. The data of the non-uniform force field for the second forcing scheme were kindly provided by



Professor K. D. Squires. The study of the effects of nonlinear drag were prompted by a discussion with Professor Renwei Mei. This research was supported by a DARPA-URI award N00014-86-K0754 and the Office of Naval Research through award N00014-91-J-1340. The computations were done at the Pittsburgh Supercomputing Center. We thank R. Reddy of PSC for his assistance in parallelizing the code on CRAY Y-MP/832.

## REFERENCES

- AUTON, T. R., HUNT, J. C. R. & PRUD'HOMME, M. 1988 The force exerted on a body in inviscid unsteady nonuniform rotational flow. *J. Fluid Mech.* **197**, 241–257.
- BALACHANDAR, S. & MAXEY, M. R. 1989 Methods for evaluating fluid velocities in spectral simulations of turbulence. *J. Comput. Phys.* **83**, 96–125.
- BENDAT, J. S. & PIERSOL, A. G. 1971 *Random Data: Analysis and Measurement Procedures*. Wiley-Interscience.
- BRASSEUR, J. G. & LIN, W.-Q. 1991 Structure and statistics of intermittency in homogeneous turbulent shear flow. *Advances in Turbulence 3*, pp. 3–12. Springer.
- CHANG, E. J. 1992 Accelerated motion of rigid spheres in unsteady flows at low to moderate Reynolds numbers. Ph.D. thesis, Brown University, Providence.
- CHUNG, J. N. & TROUTT, T. R. 1988 Simulations of particle dispersion in an axisymmetric jet. *J. Fluid Mech.* **186**, 199–222.
- CLIFT, R., GRACE, J. R. & WEBER, M. E. 1978 *Bubble, Drops, and Particles*. Academic Press.
- COMTE-BELLOT, G. & CORRSIN, S. 1971 Simple Eulerian time correlation of full- and narrow-band velocity signals in grid-generated, 'isotropic' turbulence. *J. Fluid Mech.* **48**, 273–337.
- CROWE, C. T., GORE, R. & TROUTT, T. R. 1985 Particle dispersion by coherent structures in free shear flows. *Particulate Sci. Tech.* **3**, 149–158.
- CSANADY, G. T. 1963 Turbulent diffusion of heavy particles in the atmosphere. *J. Atmos. Sci.* **20**, 201–208.
- DAVIS, R. H. & ACRIVOS, A. 1985 Sedimentation of noncolloidal particles at low Reynolds numbers. *Ann. Rev. Fluid Mech.* **17**, 91–118.
- DOMARADZKI, J. A. 1992 Nonlocal triad interactions and the dissipation range of isotropic turbulence. *Phys. Fluids A* **4**, 2037–2045.
- ESWARAN, E. & POPE, S. B. 1988 An examination of forcing in direct numerical simulations of turbulence. *Comput. Fluids* **16**, 257–278.
- FUNG, J. C. H. 1990 Kinematic simulation of turbulent flow and particle motions. PhD dissertation, University of Cambridge.
- FUNG, J. C. H., HUNT, J. C. R., MALIK, N. A. & PERKINS, R. J. 1992 Kinematic simulation of homogeneous turbulence by unsteady random Fourier modes. *J. Fluid Mech.* **236**, 281–318.
- GEORGE, W. K. 1992 The decay of homogeneous isotropic turbulence. *Phys. Fluids A* **4**, 1492–1509.
- HINZE, J. O. 1975 *Turbulence*. McGraw-Hill.
- HUNT, J. C. R., BUELL, J. C. & WRAY, A. A. 1987 Big whorls carry little whorls. *Proc. 1987 Summer Program*, Rep. CTR-S87, Stanford University, California.
- HWANG, P. A. 1985 Fall velocity of particles in oscillating flow. *J. Hydraul. Engng ASCE* **111** (3), 485–502.
- LÁZARO, B. J. & LASHERAS, J. C. 1992 Particle dispersion in the developing free shear layer. Part 2. Forced flow. *J. Fluid Mech.* **235**, 179–221.
- LONGMIRE, E. K. & EATON, J. K. 1992 Structure of a particle-laden round jet. *J. Fluid Mech.* **236**, 217–257.
- MAXEY, M. R. 1987 The gravitational settling of aerosol particles in homogeneous turbulence and random flow fields. *J. Fluid Mech.* **174**, 441–465.
- MAXEY, M. R. & CORRSIN, S. 1986 Gravitational settling of aerosol particles in randomly oriented cellular flow fields. *J. Atmos. Sci.* **43**, 1112–1134.
- MAXEY, M. R. & RILEY, J. J. 1983 Equation of motion for a small rigid sphere in a nonuniform flow. *Phys. Fluids* **26**, 883–889.

- MEEK, C. C. & JONES, B. G. 1973 Studies of the behavior of heavy particles in a turbulent fluid flow. *J. Atmos. Sci.* **30**, 239–244.
- MEI, R. 1990 Particle dispersion in isotropic turbulence and unsteady particle dynamics at finite Reynolds number. PhD thesis, University of Illinois at Urbana-Champaign, Urbana, Illinois.
- MEI, R., ADRIAN, R. J. & HANRATTY, T. J. 1991 Particle dispersion in isotropic turbulence under Stokes drag and Basset force with gravitational settling. *J. Fluid Mech.* **225**, 481–495.
- NIR, A. & PISMEN, L. M. 1979 The effect of a steady drift on the dispersion of a particle in turbulent fluid. *J. Fluid Mech.* **94**, 369–381.
- ODAR, F. & HAMILTON, W. S. 1964 Forces on a sphere accelerating in a viscous fluid. *J. Fluid Mech.* **18**, 302–314.
- PRUPPACHER, H. R. & KLETT, J. D. 1978 *Microphysics of Clouds and Precipitation*, pp. 464–541. Dordrecht: The Netherlands.
- REEKS, M. W. 1977 On the dispersion of small particles suspended in an isotropic turbulent fluid. *J. Fluid Mech.* **83**, 529–546.
- REEKS, M. W. 1980 Eulerian direct interaction applied to the statistical motion of particles in a turbulent fluid. *J. Fluid Mech.* **97**, 569–590.
- RILEY, J. J. & PATERSON, G. S. 1974 Diffusion experiments with numerically integrated isotropic turbulence. *Phys. Fluids* **17**, 292–287.
- RIVERO, M. 1991 A numerical investigation of the forces exerted on a spherical body by an accelerated flow. PhD thesis, Institut National Polytechnique de Toulouse.
- RUETSCH, G. R. & MAXEY, M. R. 1991 Small-scale features of vorticity and passive scalar fields in homogeneous isotropic turbulence. *Phys. Fluids A* **3**, 1587–1597.
- RUETSCH, G. R. & MAXEY, M. R. 1992 The evolution of small-scale structures in homogeneous isotropic turbulence. *Phys. Fluids A* **4**, 2747–2760.
- SCHÖNEBORN, P.-R. 1975 The particle interaction between a single particle and an oscillating fluid. *Intl J. Multiphase Flow* **2**, 307–317.
- SHE, Z.-S., JACKSON, E. & ORSZAG, S. A. 1990 Intermittent vortex structures in homogeneous turbulence. *Nature* **344**, 226.
- SNYDER, W. H. & LUMLEY, J. L. 1971 Some measurements of particle velocity autocorrelation functions in a turbulent flow. *J. Fluid Mech.* **48**, 41–71.
- SQUIRES, K. D. & EATON, J. K. 1991a Measurements of particle dispersion from direct numerical simulations of isotropic turbulence. *J. Fluid Mech.* **226**, 1–35.
- SQUIRES, K. D. & EATON, J. K. 1991b Preferential concentration of particles by turbulence. *Phys. Fluids A* **3**, 1169–1178.
- STEWART, R. W. & TOWNSEND, A. A. 1951 Similarity and self-preservation in isotropic turbulence. *Phil. Trans. R. Soc. Lond.* **243 A**, 359.
- TUNSTALL, E. B. & HOUGHTON, G. 1968 Retardation of falling spheres by hydraulic oscillations. *Chem. Engng Sci.* **23**, 1067–1081.
- VAN ATTA, C. W. & ANTONIA, R. A. 1980 Reynolds number dependence of skewness and flatness factors of turbulent velocity derivatives. *Phys. Fluids A* **23**, 252–257.
- WANG, L.-P., MAXEY, M. R., BURTON, T. D. & STOCK, D. E. 1992 Chaotic dynamics of particle dispersion in fluids. *Phys. Fluids A* **4**, 1789–1804.
- WANG, L.-P. & STOCK, D. E. 1993 On the dispersion of heavy particles by turbulent motion. *J. Atmos. Sci.* **50**, 1897–1913.
- WELLS, M. R. & STOCK, D. E. 1983 The effects of crossing trajectories on the dispersion of particles in a turbulent flow. *J. Fluid Mech.* **136**, 31–62.
- YEH, F. & LEI, U. 1991 On the motion of small particles in a homogeneous isotropic turbulent flow. *Phys. Fluids A* **3**, 2571–2586.
- YEUNG, P. K. & POPE, S. B. 1989 Lagrangian statistics from direct numerical simulations of isotropic turbulence. *J. Fluid Mech.* **207**, 531–586.
- YUDINE, M. I. 1959 Physical considerations on heavy-particle dispersion. *Adv. Geophys.* **6**, 185–191.